

Master Thesis

The Effects of Dark Matter on Gravitational Lensing Properties of Galaxy Clusters

Martijn van Beek

14th August 2013

Supervisors

W. Beenakker
Theoretical High Energy Physics
Radboud University Nijmegen
Nijmegen, the Netherlands

G. Lewis
Sydney Institute for Astronomy
University of Sydney
Sydney, Australia

Radboud University Nijmegen



Summary

Dark matter is one of the main components in the universe. The type of dark matter influences the amount of structure in the galaxy clusters. A cluster in a universe described by the standard cosmological model with cold dark matter (CDM) will have less structure compared to an equivalent model with warm dark matter (WDM). This report is a pilot study to investigate the possibility of distinguishing between these two types of galaxy clusters, based on their gravitational lensing effects. A cluster is taken from two cosmological simulations of both cosmologies. This three-dimensional structure is rotated to see how the gravitational lensing properties change with orientation. These properties include the maximum value for the convergence, the ellipticity, the caustic areas, the shear characterization parameters and the magnification probability distribution.

By relating the convergence and the ellipticity, it became clear that more structure is present in the WDM cluster compared to the CDM one. This is according the expectations. Also the analysis of other quantities confirmed this.

There were a couple of promising ways of analysis which may have the ability to identify the type of cosmology. The characterization of the shear resulted in parameters that showed some nice relations for both cosmologies. More investigation is needed to determine the potential of this method as other characterizations could result in parameters that relate even better with other quantities.

Moreover, the results showed an important hint to a different behaviour between the two cosmologies. The magnification probability distributions at high magnifications of the CDM cluster behave conform the expected power law with an exponent of -3 . Whereas the WDM cluster resulted in an exponent -4 .

Only one cluster per cosmology was used, so more clusters are needed to give a conclusive answer to the question if the types of cosmologies can be distinguished from their gravitational lensing effects. Besides that and the characterization of the shear, future research could also include the dependence of the results upon the red shifts of the lens and the source. In this report only one set of values is used, but clusters are actually distributed over a whole range of red shifts, which would result in different gravitational lensing properties.

Contents

Summary	i
Contents	iii
1 Introduction	1
1.1 Dark matter	1
1.2 Gravitational lensing	3
1.3 Goal and plan	5
2 Theory of gravitational lensing	6
2.1 Theoretical basics	6
2.2 Effects on images	12
3 Calculation aspects	21
3.1 Input	21
3.2 Implementation	23
3.3 Getting results	28
3.4 Expected results	32
4 Results	36
4.1 Rotations	36
4.2 Magnification probability distribution	51
4.3 Discussion	59

5	Conclusions	65
	References	67
	Appendix A Methods used	69
A.1	Random rotation matrix	69
A.2	Ellipticity	70
A.3	Algorithm <code>FillGaps</code>	72
A.4	Algorithm <code>FindBlobs</code>	73
	Appendix B Supplementary tables and figures	75
B.1	Rotations	75
B.2	Magnification probability distribution	78

1 Introduction

This chapter will give an overview and bigger picture of the subjects that are discussed in this report. This includes an introduction to dark matter and gravitational lensing. In the end the goal of this research will be formulated.

1.1 Dark matter

A big question in physics is what dark matter actually is. There is not much known about dark matter. Even (in)direct measurements do not give a conclusive answer. Nevertheless, there are some strong pieces of evidence that dark matter is there. At least two pieces of evidence will be outlined here.

When looking at a galaxy, the thing that is seen is a rotating disk made of stars. So each star has a certain velocity with which it goes around the centre. By equating Newton's law of universal gravitation and the centripetal force, an expression for this orbital velocity v can be found. The result for v is, as a function of its distance to the centre r and the mass enclosed by the (circular) orbit $M(< r)$,

$$v(r) = \sqrt{\frac{GM(< r)}{r}}$$

where G is the gravitational constant. (This equation assumes a spherical mass distribution, which suffices for this example.) Outside the region that contains all the mass in the galaxy, M becomes a constant and so the velocity will only depend on the distance like $v \propto r^{-1/2}$. This means that stars in the outskirts of the galaxy should rotate slower for increasing distance. But many measurements (see [1] and [2]) show that those outer stars all rotate with an approximately constant velocity. Bearing in mind that they are located far away from the great majority of stars in the galaxy, this means that there is more mass than only the visible matter suggests. This extra mass can be accredited to the dark matter, named after the fact that it does not emit any electromagnetic radiation.

The problem of missing matter is not the only indication for the possibility that there is dark matter out there. The same problem arises when looking at the velocity of galaxies in clusters of galaxies. Another nice example, in which dark matter manifests itself as missing matter, is gravitational lensing. This lensing is based on the principle that light is bent by mass. As galaxies and galaxy clusters contain a lot of mass, they act as gravitational lenses and so light from behind the lens is bent towards the observer. Gravitational lensing is a powerful tool, but more on this will be given in the following section.

So, huge amounts of dark matter are contained in galaxies and clusters of galaxies. One of the latest results from the Planck collaboration, as stated in [3], is that dark matter makes up 27% of the energy budget of the universe at the present time. The question, what is actually known about this substance, will be answered in the remainder of this section.

Assuming dark matter is made of particles, many measurements tried to measure the properties of these particles (in)directly. Besides some general properties, no other quantities could be defined for dark matter particles. A general feature of the particles is that they interact only very weakly with ordinary matter. This can be deduced from the fact that it emits no light and also in particle accelerator experiments nothing has been found so far. One clear thing is that the dark matter particles influence ordinary matter mainly via the gravitational force.

Even the mass of those dark matter particles remains uncertain. Different kinds of particles can be specified according to their kinetic energy (at the time when the universe made the transition from matter dominated to radiation dominated). Relativistic dark matter particles will be referred to as hot dark matter (HDM). Conversely cold dark matter (CDM) is defined by particles with only small, non-relativistic velocities. Naturally, there is also an intermediate range of particle velocities and these particles are called warm dark matter (WDM). These types of dark matter have big influences on the structure formation in the universe.

Structure in the universe forms from collapsing regions where the density is higher than the average, overall density. In case of HDM, first large structures will form, which split up after some time, resulting in more smaller structures. The HDM particles have too much kinetic energy to immediately form gravitationally bound small structure as they would tear apart the small clumps. All this means that HDM would prevent early formation of low-mass structures, such as dwarf galaxies. Conversely in a universe with CDM, first galaxies will form from the collapse of gas. After the universe cools down further, these galaxies will attract each other to form the clusters.

Observations of galaxies already present at high red shifts (early in the universe), favour a cosmology with CDM. Such a universe, also including dark energy Λ (needed

for an accelerating universe), forms the standard model of cosmology denoted by Λ -CDM. More on this model can be found in section 3.1.

There is not a well-defined boundary separating cold and warm dark matter. Their influence on the structure formation manifests itself in the amount of structure. As explained, in a CDM cosmology cluster there will be more small-scale structures (dwarf galaxies) and fewer large-scale structures (parts in a cluster) when compared to a WDM cosmology cluster. Maybe clusters from the two cosmologies can be distinguished with the use of gravitational lensing.

1.2 Gravitational lensing

As already explained in the previous section, gravitational lensing is a phenomenon that can occur because light bends as it comes near a mass. This is schematically shown in figure 1.1¹. The figure shows a massive galaxy cluster that deforms space. Rays of light, that are coming from a galaxy located behind the cluster, will not follow a straight line any more as space is curved. This makes the light bend towards the mass before it reaches the observer. These rays of light form images that can be very different from the image of the source galaxy when there would not be a lens.

Some examples of actual observations of gravitational lensing are shown in figure 1.2. In the picture on the left (figure 1.2a²) light from a distant quasar/galaxy bends around a massive galaxy cluster (called CL0024+1654). This is seen as multiple images positioned around the big cluster. In a special case, gravitational lensing can even result in a ring as image. This ring is called an Einstein ring and an example is shown in figure 1.2b³. The object name is LRG 3-757 and it is an almost complete Einstein ring.

Gravitational lensing can occur on different scales, which can be divided into three regimes. First, there is strong lensing of which examples are given in the previous paragraph. As the name indicates, in this regime the lensing is strong enough to produce multiple images, sometimes in combination with highly elongated images like arcs. In order to get these strong effects a very massive lens is needed such as a massive galaxy or a cluster of galaxies. In the second regime only weak lensing occurs in which single images are only deformed and become elliptical. In case of strong lensing, weak lensing effects are also part of those effects. Finally, there is also lensing due to compact objects like planets and stars. This phenomenon is called microlensing. In this report the strong and so also the weak lensing regimes will be probed. A more detailed discussion about gravitational lensing is given in chapter 2.

¹Image credit: NASA, ESA and L. Calçada

²Image credit: W.N. Colley and E. Turner (Princeton University), J.A. Tyson (Bell Labs, Lucent Technologies) and NASA/ESA.

³Image credit: ESA/Hubble and NASA.

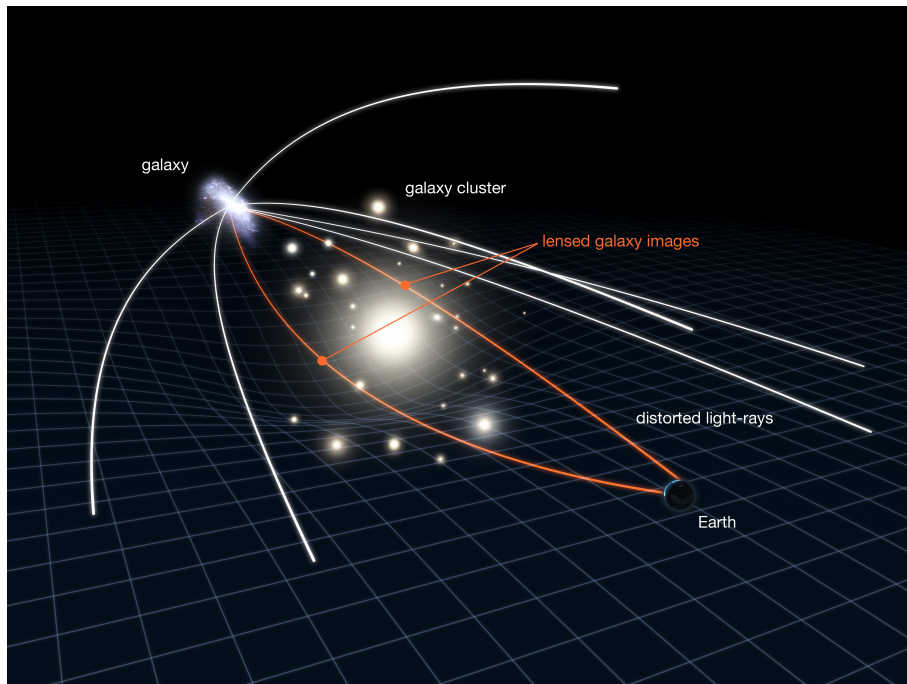
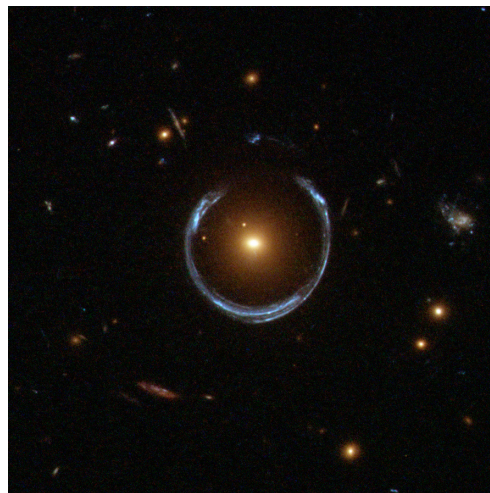


Figure 1.1: Schematic illustration of a situation in which gravitational lensing occurs.



a



b

Figure 1.2: Examples of gravitational lensing (in blue) with a) distorted images and b) an almost complete Einstein ring.

One of the reasons why gravitational lensing is such an important tool is that dim objects at high red shifts become observable as they get magnified by a gravitational lens. Another reason is that it can be used to determine some properties of the lens itself. A common method is to look at some cluster (or heavy galaxy) and identify all images of the galaxies that are visible on the picture. Of all these objects the size, shape and/or ellipticity can be measured. Also multiple images corresponding to one source can be identified. All this information can be used to create a shear map. The quantity shear will be discussed in the following chapter, but it holds information about the deformation of the images due to the lens. Then, from this shear map a mass reconstruction of the lens can be made. When the mass distribution of the lens is known, then all its lensing properties can be calculated.

1.3 Goal and plan

Now that is known what gravitational lensing can be used for and what the influence is of dark matter on structure formation, a research goal can be defined:

Investigate the possibility of making a distinction between galaxy clusters originating from cold and warm dark matter cosmology by means of gravitational lensing effects.

In order to achieve this, the gravitational lensing properties are calculated for two simulated galaxy clusters. These clusters are the results of cosmological structure formation simulations, just as it would have happened in the universe. The difference between them is that one contains CDM, whereas the other one has WDM instead of CDM. A part of the results will consist of properties of the lens itself. Another part of the result will take a look at the effects that the lenses have on the magnification of the images. Perhaps some results will show a difference that enables to distinguish between the two different cosmologies.

The research of this report is an investigation if this kind of approach could be used as a new measurement method. If clear differences for CDM and WDM cosmologies are found, then these can be compared to observations. In this way a constraint can be given for the type of dark matter that is present in the universe.

In the following chapters, first the theory behind gravitational lensing is explained and the necessary formulae will be derived in chapter 2. Then in chapter 3 the implementation and issues of the calculations will be dealt with. In the next chapter the results and a discussion will be presented. After that the conclusions and possible outlook will be given in chapter 5. The report finishes with the list of references followed by the appendices, containing some calculational methods and supplementary figures.

2 Theory of gravitational lensing

In this chapter the situation will be sketched in which gravitational lensing occurs. Also calculations will be discussed that are needed to quantify the lensing effects. Extra attention is paid to the derived quantities that affect the images that are produced by a gravitational lens. The theory outlined in the following is based on the treatment in [4].

2.1 Theoretical basics

Deflection angle — The theory of gravitational lensing starts with the bending of light due to a certain mass distribution. As the theory of general relativity states, light will bend towards the mass as it travels through the gravitational potential of that mass. A situation is sketched in figure 2.1 which considers a ray of light bent by a point mass. The angle by which the light gets deflected when passing the mass M at a distance ξ is given by

$$\hat{\alpha} = \frac{4G}{c^2} \frac{M}{\xi}, \quad (2.1)$$

where G is the gravitational constant and c is the speed of light. When imagining a distribution of several point masses M_i at positions $\vec{\xi}_i$, then the resulting deflection angle becomes

$$\hat{\alpha}(\vec{\xi}) = \frac{4G}{c^2} \sum_i \frac{\vec{\xi} - \vec{\xi}_i}{|\vec{\xi} - \vec{\xi}_i|^2} M_i. \quad (2.2)$$

This formula assumes that all masses are laying in a geometrically-thin plane perpendicular to the line-of-sight (thin compared to the distance of the observer to the source). This will be justified further on in this section. Because of the multiple masses, the direction of deflection (towards each mass) should be included, by introducing the fraction $\frac{\vec{\xi} - \vec{\xi}_i}{|\vec{\xi} - \vec{\xi}_i|}$.

In reality the lens will be a continuous three-dimensional mass distribution. Because the lens is geometrically thin, only the projected mass distribution or surface mass density

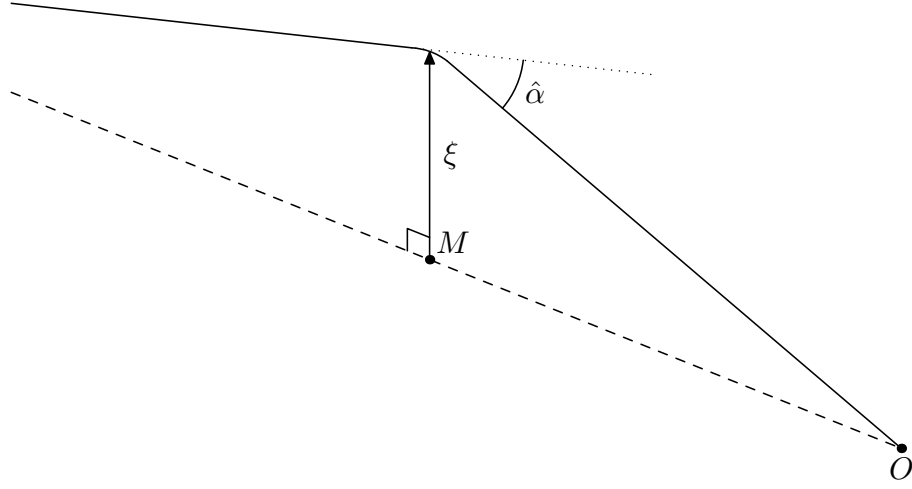


Figure 2.1: The effect of gravitational lensing by a point mass M on a ray of light (solid line), where ξ is the distance from the mass to the ray in the plane perpendicular to the line-of-sight (dashed line) and $\hat{\alpha}$ is the angle by which the light ray is bent.

Σ matters. This surface mass density is given by $\Sigma(\vec{\xi}) = \int \rho(\vec{\xi}, z) dz$, where the integral runs over the whole line-of-sight, the z -dimension (or as far as the mass distribution extends). In order to incorporate a continuous distribution, the continuum limit of (2.2) is taken

$$\hat{\alpha}(\vec{\xi}) = \frac{4G}{c^2} \int \frac{\vec{\xi} - \vec{\xi}'}{|\vec{\xi} - \vec{\xi}'|^2} \Sigma(\vec{\xi}') d^2 \vec{\xi}' \quad (2.3)$$

where $\Sigma(\vec{\xi}') d^2 \vec{\xi}'$ is the mass of an infinitesimal element of the lens. Now the integral runs over the whole lens plane (or, again, as far as the mass distribution extends).

Lens equation — With the definition of the deflection angle, now it is time to look at a more detailed situation sketch. This sketch is given in figure 2.2 in which light from a source (S) gets deflected (at point I) before it reaches the observer (O). The figure contains all necessary variables to construct the lens equation. In this equation the deflection angle $\hat{\alpha}$ is related to the angles of the source and image, β and θ respectively.

In the situation sketch it is assumed that all the angles (α , $\hat{\alpha}$, β and θ) are very small, or equivalently, the position $\eta(\xi)$ is very small compared to the distance to the source D_s (lens D_l). As a consequence the following relations can be used

$$\beta = \frac{\eta}{D_s} \quad \text{and} \quad \theta = \frac{\xi}{D_l}. \quad (2.4)$$

These distances D are angular-diameter distances and they are actually defined by formula 2.4. In general the relation $D_{ls} = D_s - D_l$ is not valid as a flat (Minkowski) space-time is not applicable for the universe on large scales.

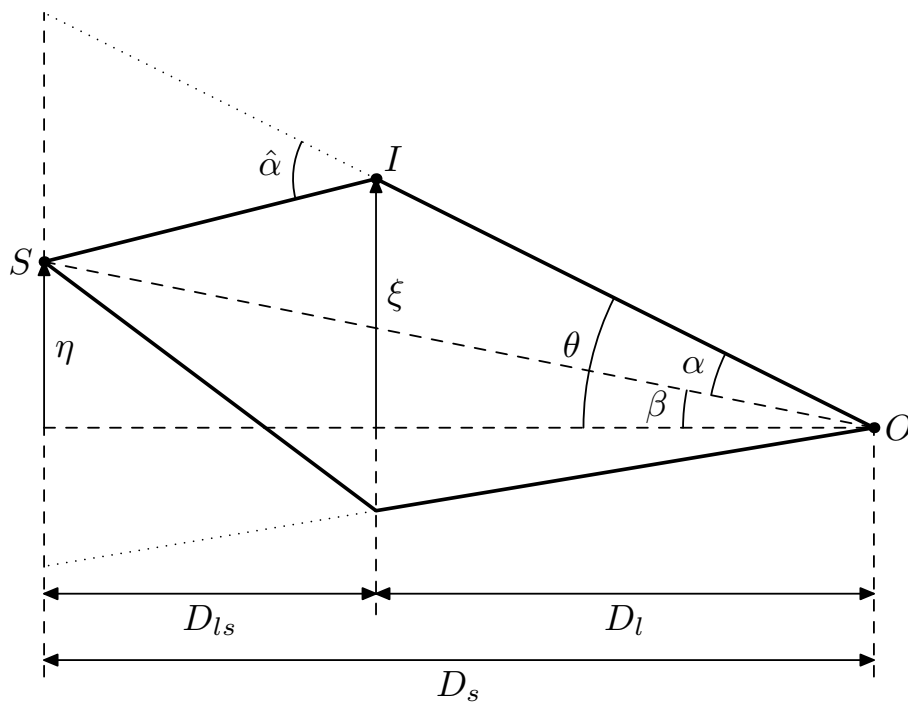


Figure 2.2: Situation sketch of a gravitational lensing system. Light (thick solid lines) from a source S is deflected at point I in the lens plane before reaching the observer O . The angles α , $\hat{\alpha}$, β and θ are related to the positions of the ray of light in the source and lens plane, η and ξ respectively, and the angular-diameter distances D .

As starting point for the lens equation the relation between the deflection angle $\hat{\alpha}$ and the positions $\vec{\eta}$ and $\vec{\xi}$ is used. It can be derived immediately from the situation sketch and is given by

$$\vec{\eta} = \frac{D_s}{D_l} \vec{\xi} - D_{ls} \hat{\alpha}(\vec{\xi}) . \quad (2.5)$$

After dividing the equation by D_s and converting the positions to their corresponding angles using (2.4), the resulting lens equation becomes (also called the ray-trace equation)

$$\vec{\beta} = \vec{\theta} - \vec{\alpha} \quad (2.6)$$

which uses the definition of the scaled (or reduced) deflection angle $\vec{\alpha} = \frac{D_{ls}}{D_s} \hat{\alpha}$. This equation can be seen in different ways. When the position of an image and the distances D are known, then the equation tells where the source is positioned. The lens equation also represents the mapping from the lens plane to the source plane. Moreover this equation can also be used to calculate the images that correspond to a certain source. Note that each solution of the equation results in one image and so multiple images can be formed as the equation can have multiple solutions.

After introduction of the critical surface mass density

$$\Sigma_{cr} = \frac{c^2}{4\pi G} \frac{D_s}{D_l D_{ls}} \quad (2.7)$$

the surface mass density Σ can be written as the convergence, also called dimensionless surface mass density

$$\kappa(\vec{\theta}) = \frac{\Sigma(D_l \vec{\theta})}{\Sigma_{cr}} . \quad (2.8)$$

Using this definition, the final expression for the scaled deflection angle becomes

$$\vec{\alpha}(\vec{\theta}) = \frac{1}{\pi} \int \frac{\vec{\theta} - \vec{\theta}'}{|\vec{\theta} - \vec{\theta}'|^2} \kappa(\vec{\theta}') d^2 \vec{\theta}' . \quad (2.9)$$

From this point on α will be called the deflection angle. As a short recapitulation of the dependencies, the whole system depends on the mass distribution of the lens. From this distribution one can calculate the convergence. Subsequently the convergence can be used to determine the deflection angle. Then the lens equation can be used to map images back to the source, or to construct images for a given source.

Deflection potential — From the identity $\vec{\nabla} \ln |\vec{r}| = \frac{\vec{r}}{|\vec{r}|^2}$ it follows that the deflection angle can be rewritten as a gradient of a potential with respect to $\vec{\theta}$ like

$$\vec{\alpha} = \vec{\nabla} \psi \quad (2.10)$$

where ψ is the logarithmic deflection potential as a function of the convergence κ ,

$$\psi(\vec{\theta}) = \frac{1}{\pi} \int \kappa(\vec{\theta}') \ln |\vec{\theta} - \vec{\theta}'| d^2\vec{\theta}' . \quad (2.11)$$

This means that the transformation from the image position θ to the source position β is a gradient mapping via

$$\vec{\beta} = \vec{\nabla} \left(\frac{1}{2} \vec{\theta}^2 - \psi(\vec{\theta}) \right) . \quad (2.12)$$

Another identity which will prove to be useful is $\Delta \ln |\vec{r}| = 2\pi\delta^{(2)}(\vec{r})$ with the Laplacian operator $\Delta = \vec{\nabla} \cdot \vec{\nabla}$ and the two-dimensional delta-function $\delta^{(2)}$. This identity applied to the potential results in

$$\Delta\psi = 2\kappa . \quad (2.13)$$

This final relation and the deflection potential will be used in the following.

Amplification matrix, shear and magnification — The lens equation can be used to construct images for a given source. So this mapping contains information about the shape of the images for a certain source. In order to know more about these images the Jacobian matrix of the lens mapping will be investigated. This matrix is defined by

$$A(\vec{\theta}) = \frac{\partial \vec{\beta}}{\partial \vec{\theta}} \quad \text{or} \quad A_{ij} = \frac{\partial \beta_i}{\partial \theta_j} \quad (2.14)$$

and is called the amplification matrix. Elements of A can be expressed in terms of the partial derivatives of the potential ψ , which are denoted by $\psi_{ij} = \frac{\partial^2 \psi}{\partial \theta_i \partial \theta_j}$. In these terms, identity (2.13) becomes $\kappa = \frac{1}{2}(\psi_{11} + \psi_{22})$. After inserting formula (2.12) (or (2.6)) and the just mentioned identity, the amplification matrix can be written as

$$\begin{aligned} A &= \begin{pmatrix} 1 - \psi_{11} & -\psi_{12} \\ -\psi_{12} & 1 - \psi_{22} \end{pmatrix} \\ &= \begin{pmatrix} 1 - \kappa - \gamma_1 & -\gamma_2 \\ -\gamma_2 & 1 - \kappa + \gamma_1 \end{pmatrix} \end{aligned} \quad (2.15)$$

where we introduced

$$\gamma_1 = \frac{1}{2}(\psi_{11} - \psi_{22}) \quad \text{and} \quad \gamma_2 = \psi_{12} = \psi_{21} \quad (2.16)$$

which are the components of the property called shear. It must be stressed that the shear is not a vector even though this might be suggested by the term component. The total amount of shear is defined by $\gamma = \sqrt{\gamma_1^2 + \gamma_2^2}$ (often just referred to as shear). Another thing to note is that after calculation of the amplification matrix, the convergence is part of the result again. (So this is exactly the same as the convergence put into the calculation via formula 2.11.)

Finally, some characteristic properties of the amplification matrix will be calculated. The eigenvalues of the amplification matrix are given by

$$\lambda_t = 1 - \kappa - \gamma \quad \text{and} \quad \lambda_r = 1 - \kappa + \gamma \quad (2.17)$$

where the subscripts stand for tangential and radial, respectively. These terms will become clear in the following section. As the amplification matrix is a Jacobian matrix, its determinant describes the area distortion of the lens mapping from the image to the source. This determinant is given by

$$\det A = \lambda_t \lambda_r = (1 - \kappa)^2 - \gamma^2 \quad (2.18)$$

and so this means that an infinitesimal area in the source plane is magnified by a factor of

$$\mu = \frac{1}{|\det A|} = \frac{1}{|(1 - \kappa)^2 - \gamma^2|} . \quad (2.19)$$

Note that the amplification matrix and all its terms are functions of the position θ .

Convolution — At this point it is clear how to calculate the main properties, such as the deflection angle and the shear. But instead of straightforwardly calculating the integrals in the partial derivative of the potential ψ , there is a much more efficient way of doing this. Recalling the formula for the deflection angle

$$\vec{\alpha}(\vec{\theta}) = \frac{1}{\pi} \int \frac{\vec{\theta} - \vec{\theta}'}{|\vec{\theta} - \vec{\theta}'|^2} \kappa(\vec{\theta}') d^2 \vec{\theta}' , \quad (2.9)$$

it can be seen that this is exactly the convolution between the function $\frac{\vec{r}}{|\vec{r}|^2}$ and the convergence κ . This means that when moving to Fourier space, the following (convolution) theorem can be applied:

$$h(x) = \int f(x')g(x - x') dx' = (f * g)(x) \rightarrow \mathcal{F}(h(x)) = \mathcal{F}(f(x))\mathcal{F}(g(x)) \quad (2.20)$$

where \mathcal{F} represents the Fourier transform. With this theorem, the deflection angle can be calculated by

$$\vec{\alpha}(\vec{\theta}) = \frac{1}{\pi} \mathcal{F}^{-1} \left(\mathcal{F} \left(\frac{\vec{\theta}}{|\vec{\theta}|^2} \right) \mathcal{F}(\kappa(\vec{\theta})) \right) . \quad (2.21)$$

This function $\frac{\vec{\theta}}{|\vec{\theta}|^2}$ is called the convolution kernel and in this case it is used to calculate the deflection angle. Note that the x and y direction of the deflection angle come from the corresponding direction of the kernel,

$$\frac{\theta_1}{\theta_1^2 + \theta_2^2} \quad \text{and} \quad \frac{\theta_2}{\theta_1^2 + \theta_2^2} \quad (2.22)$$

respectively. Similarly, the calculation of the amplification matrix requires kernels coming from the second derivatives of the deflection potential ψ . The derivatives are given by $\frac{\partial^2}{\partial\theta_i \partial\theta_j} \ln |\vec{\theta}|$ and so the kernels corresponding to ψ_{11} , ψ_{12} and ψ_{22} are

$$\mp \frac{\theta_1^2 - \theta_2^2}{(\theta_1^2 + \theta_2^2)^2} \quad \text{and} \quad -2 \frac{\theta_1 \theta_2}{(\theta_1^2 + \theta_2^2)^2}. \quad (2.23)$$

As mentioned previously, the argument to do the calculations in Fourier space is efficiency. It will require considerably less computation time as will be demonstrated in the following. Two matrices of size $N \times N$ will be considered in this example. When doing the straightforward convolution by means of an integral, then the calculation of each output element needs $\mathcal{O}(N^2)$ multiplications (being the most time-expensive operation). So, for the complete convolution of N^2 output elements, $\mathcal{O}(N^4)$ operations are done. The other method of performing the convolution is by transforming to and from Fourier space. The Fast Fourier Transform (FFT) can be used for this. This starts with the calculation of the one-dimensional transform for each row and column, each one consisting of N elements and needing $\mathcal{O}(2N \log_2(N))$ calculations. For the two-dimensional transform of a whole matrix with N rows and N columns, the computation consists of $\mathcal{O}(4N^2 \log_2(N))$ multiplications. Of course there are two matrices to be transformed and the result has to be transformed back, so then the calculation time is of order $\mathcal{O}(12N^2 \log_2(N))$. When also incorporating the element-wise multiplication of the two complex matrices, then this results in a total of $\mathcal{O}(12N^2 \log_2(N) + 4N^2)$ operations. So now it can be determined for which values of N it will be more efficient to use the Fourier transform, namely when $12 \log_2(N) + 4 < N^2 \rightarrow N > 5.89\dots$ which is certainly too small for our purpose. In fact matrices will be used of size $N = 2^{10} = 1024$.

2.2 Effects on images

As the basics are done, it is time to look at the effects of the individual properties on the gravitationally lensed images. Those images are (de)magnified and distorted versions of the source due to many effects. In this section some effects are highlighted. The two main quantities derived in the previous section are the convergence and the shear. They influence the size and shape of the images as will be explained in this section. Combinations of κ and γ resulted in the amplification matrix eigenvalues λ_t and λ_r . As will be shown, these λ 's will play an important role in how many images are produced.

Convergence and shear — A bundle of photons deflected by mass is affected by both the mass located inside the bundle, as well as the mass outside of the bundle. The effect of the mass inside the bundle of photons is represented by the convergence and shear is due to the mass distribution outside the bundle. These effects are depicted in figure 2.3

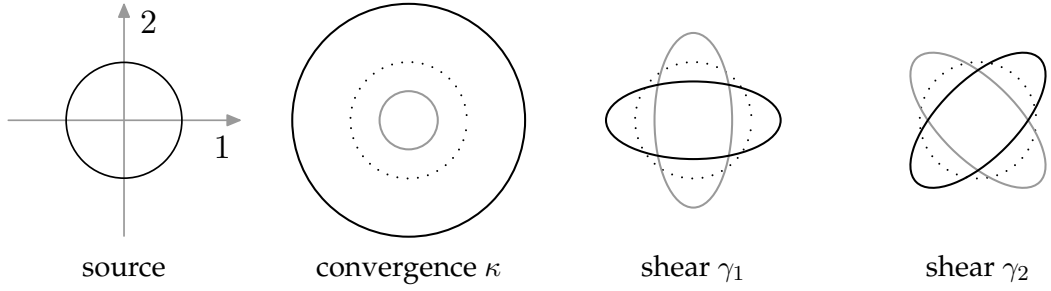


Figure 2.3: The possible effects of convergence and shear on the size and shape of images. From left to right. First an image is shown of the unlensed source. The second image depicts the magnified (demagnified) image of the source in black (grey). The third situation represents the consequences of shear due to $\gamma_1 > 0$ ($\gamma_1 < 0$) in black (grey). Similarly the fourth picture shows the effect of $\gamma_2 > 0$ ($\gamma_2 < 0$) as the black (grey) curve. In the last three figures the original source is shown as a dotted circle. See the text for more details.

and described in the following paragraphs.

The images of a circular source are (de)magnified due to the convergence, but distortions in shape are caused by shear, as figure 2.3 shows. Recalling that the magnification is given by $\mu = \frac{1}{|(1-\kappa)^2 - \gamma^2|}$, then a $\mu > 1$ can be expected when $0 < \kappa < 2$ (roughly). This assumes that the shear is small, which is approximately true at the centre of a galaxy cluster where the convergence is also maximal. In this same situation, when $\kappa > 2$, then the images will be decreased in size and so $\mu < 1$.

A non-zero shear results in a distorted/elongated version of the source. If the first component of the shear, γ_1 , is greater than one, then this results in an image stretched in the horizontal direction (denoted by 1), as shown in figure 2.3. An image that is stretched along the vertical axis (2) corresponds to $\gamma_1 < 1$. Similarly as for γ_1 , the component γ_2 has the same effects, but with the difference that the directions are rotated 45° anticlockwise, so the images are stretched along the diagonals.

To get a better understanding of the relation between κ and γ , a more intuitive representation of the shear is needed. This can be done by making a shear map which uses an alternative representation of the shear. The two components of shear can be combined into an amplitude $\gamma = \sqrt{\gamma_1^2 + \gamma_2^2}$ and an angle $\phi = \frac{1}{2} \arctan \frac{\gamma_1}{\gamma_2}$. Although shear itself is not a vector, it can be represented by a vector with a direction ϕ and magnitude γ . These vectors represent the direction ϕ and magnitude γ of the elongation of the images and they are used to construct a shear map. The map will show "compass needles" (headless arrows) to mark the stretching of an image at that position.

As an example of the construction of a shear map, figure 2.4 shows a convergence map, both shear components and the superposition of the convergence and the shear

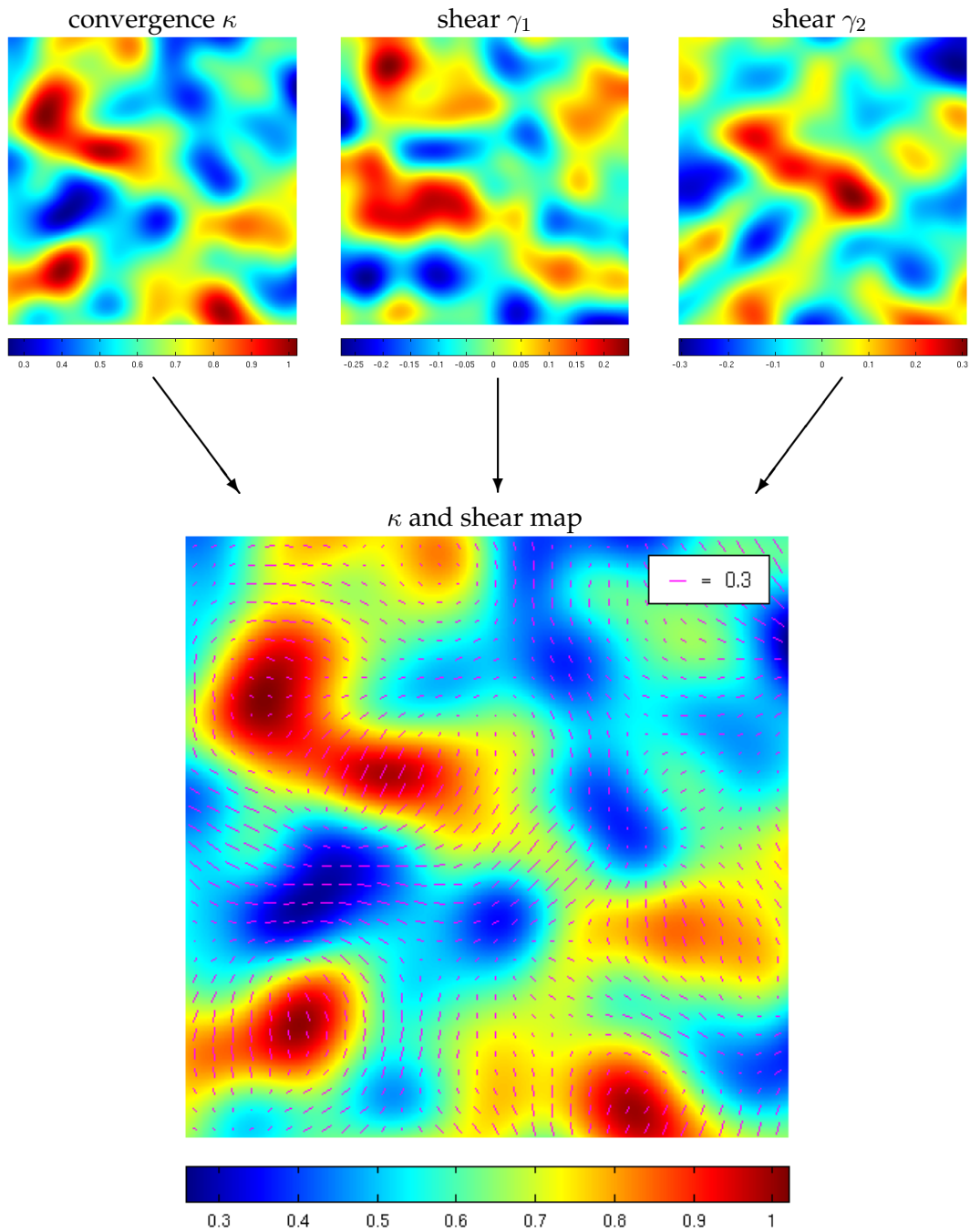


Figure 2.4: A convergence map (top left) with the two corresponding shear components (first at top middle, second at top right), used to illustrate the relation between them. The bottom plot shows again the convergence map (coloured background), but with the shear map (magenta coloured compass needles) printed on top of it, where the length of the line in the legend depicts the magnitude of the shear. For more details, see the text.

map. The example shows a region of low γ_1 (like the bottom left corner) that corresponds to vertical lines in the shear map. A region of high γ_2 (around the centre) corresponds to inclining diagonal lines in the shear map.

With this shear map, it becomes much easier to investigate the relation between convergence and shear. When looking at the combined map of the convergence and shear (bottom image of figure 2.4), some patterns can be recognized. Firstly the shear map curls around peaks in the convergence map (bottom left corner). Secondly the figure shows that the shear points towards the minima of the convergence. A less clear feature is that a saddle point in the convergence makes the shear point to the lower parts. An example of this is given in the centre of the map where a long ridge of high convergence results in a shear map aligned perpendicular to the ridge.

A little remark about the convergence map given in figure 2.4 is that the given distribution is not at all representative for the galaxy clusters used in this report. It just served its purpose well as an illustrating example. The simulated galaxy clusters in this report both have a high convergence in the centre and it decreases rather smoothly going away from the centre, similar to a bell shape.

Critical lines and caustics — Besides their individual effects on images, the convergence and shear are also combined in the formulas for the eigenvalues of the amplification matrix, which are used to investigate another effect. Those amplification matrix eigenvalues $\lambda_t = 1 - \kappa - \gamma$ and $\lambda_r = 1 - \kappa + \gamma$ are combined in the formula for the magnification, $\mu = \frac{1}{|\det A|} = \frac{1}{|\lambda_t \lambda_r|}$. Effects on images can be better understood when investigating these quantities and defining critical lines and caustics.

The eigenvalues λ can have either sign and so they can be zero. In case an eigenvalue would vanish, then the magnification becomes infinite. The line, drawn in the lens plane (using coordinates θ), across which λ_t changes sign, is called the tangential critical line. Similarly the line where $\lambda_r = 0$ is called the radial critical line (in the lens plane). The corresponding lines in the source plane (using coordinates β) are called the caustics.

To show the effect of these lines, a few examples of lensing events are given in figure 2.5. The lens used in this figure has a circularly symmetric mass distribution. The figure shows six panels in which the position of the source is varied, resulting in different (sometimes multiple) images. The specific situations will be discussed shortly, but first the design of the figure will be explained. In each panel the plane on the left contains the source and caustics. This plane will be called the source plane. The plane on the right shows the critical lines and the images and is therefore the image plane. Note that despite its name, the source (image) plane is not a plane, but rather the view without (with) the presence of a lens. The two planes have the same angular size.

Due to the circularly symmetric distribution used in figure 2.5, the critical lines and caustics are circular too. The caustic shaped as a circle (on the left in each panel) is the

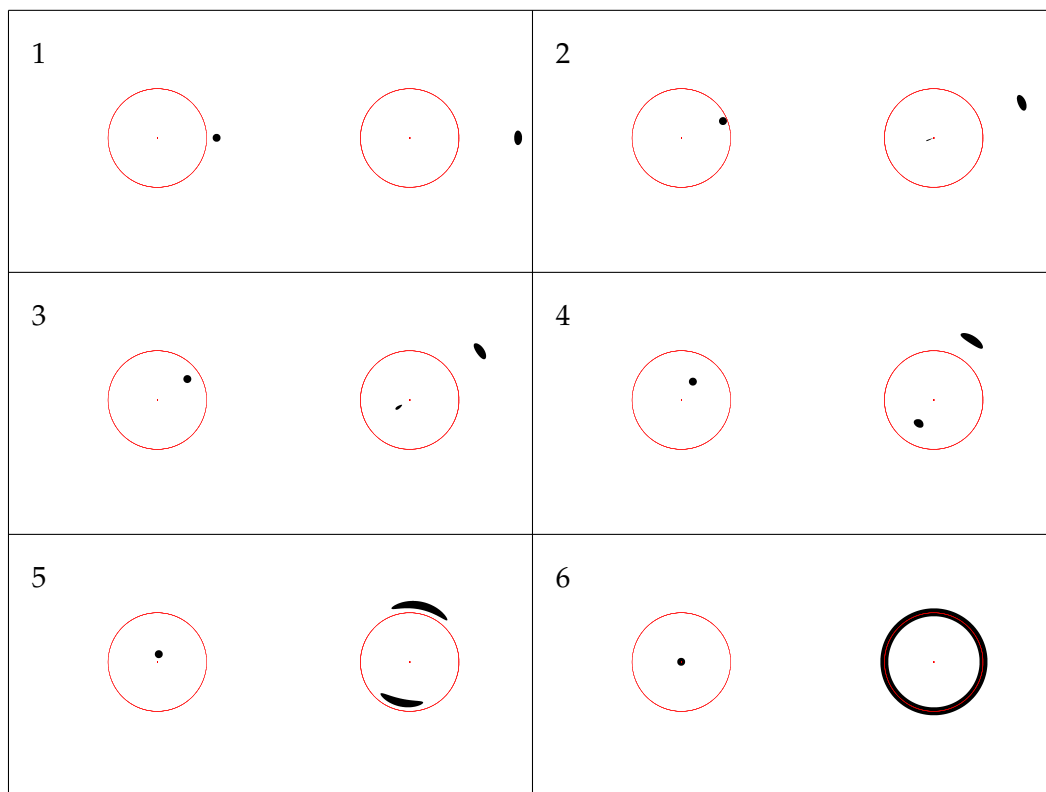


Figure 2.5: The images that are gravitationally lensed by a circular mass distribution. Each panel shows the source plane on the left, displaying the position of the source (black) and the caustics of the lens (red). Similarly the right side of each panel shows the images (black) and critical lines (red) in the image plane.

radial caustic and the corresponding radial critical line is a degenerate point at the origin (on the right in each panel). Similarly, the tangential caustic is the degenerate point at the origin in the source plane. The tangential critical line associated with this caustic is the circle shown in the image plane. The behaviour of the images near critical lines is indicated by the name of the lines as will be explained. The six specific situations are now discussed briefly.

1. The source is located outside the radial caustic. The only image is a slightly magnified ($\mu > 1$) and distorted version of the source.
2. In this situation the source is only just contained within the radial caustic. Besides the outer image, which is increased in size, a second image seems to emerge from the degenerate radial critical point at the origin. This second image shows a demagnified ($\mu < 1$) version of the source.
3. Now the source is fully contained within the outer caustic and so the more central image is not connected to the degenerate critical point any more. Both images got bigger in comparison with the previous situation.
4. As the source is moving closer to the origin, consequently both images (in- and outside the tangential critical line) are getting bigger and more stretched. By now both images have a magnification greater than one.
5. The source is almost in contact with the tangential caustic (the degenerate point at the origin) and therefore the two images start to curl along the tangential critical line to form strongly elongated arcs with $\mu \gg 1$.
6. As the source coincides with the tangential caustic point, the images merged into an Einstein ring. This feature is only possible for a (almost perfectly) circularly symmetric distribution.

The Einstein ring has a certain radius, which only depends on the total mass of the cluster and the distances. The Einstein radius is defined by

$$\theta_E = \sqrt{\frac{4GM}{c^2} \frac{D_{ls}}{D_l D_s}}.$$

From this example of a circular distribution, it is already becoming clear what the caustics and critical lines represent. When a source is located on or near the tangential caustic, then the images will be stretched along the tangential critical line. So images are elongated in the tangential direction of the critical line. Whereas a source on or near the radial caustic gives rise to a second image stretched perpendicular to the radial critical line.

All this can be studied in more detail with another example, now using an elliptical distribution (with major axis aligned with the vertical axis). In this case the critical lines and caustics have shapes as in figure 2.6. The radial caustic has become an ellipse-like shape, just as the tangential critical line, which were circles in case of a circular distribution. There is a big change in the shape of the tangential caustic, which went from a degenerate point to a diamond-like structure. For each depicted situation in the figure some details are given.

1. Just as for the circularly symmetric case, a source located outside the radial caustic results in only one image with a magnification larger (or equal) than one ($\mu > 1$).
2. The radial critical line is still a degenerate point, so a second image seems to come out of this point as the source moves across the radial caustic.
3. Now the source touches the tangential caustic and consequently a third image emerges from the critical line.
4. The source is still, only just, on the tangential caustic, so there are three images. But the source moved across the caustic and so the image is strongly elongated with a magnification much larger than one ($\mu \gg 1$).
5. At this point the source is fully contained within the tangential caustic, causing the third image to split up in two separate images. Still both images have a high magnification.
6. Now the source coincides with the origin and so the images are point-symmetric around the centre. Because of the absence of a degenerate point as tangential caustic, no Einstein ring can be formed.

Although not shown in any example, the radial caustic can be smaller than the tangential caustic. It can even disappear, leaving only one (long) tangential caustic. The tangential caustic says something about the shape of the distribution. While the radial caustic is more about the total mass of the distribution as it becomes bigger for a higher convergence. This is because the quantity λ_r (formula 2.17) will be zero farther away from the centre if the convergence is higher (assuming a constant shear).

Even though the specific examples will not be used in the rest of this report, one feature will be clarified in the following. The first, circular model that was used is called the non-singular isothermal sphere (NIS). Similarly the second, elliptical one is called the non-singular isothermal ellipsoid (NIE). The convergence for these models (see [5]) is given by

$$\kappa_{NIS}(\vec{\theta}) = \frac{1}{2\sqrt{\theta_1^2 + \theta_2^2 + x_c^2}} \quad \text{and} \quad \kappa_{NIE}(\vec{\theta}) = \frac{\sqrt{f}}{2\sqrt{\theta_1^2 + f^2\theta_2^2 + x_c^2}}, \quad (2.24)$$

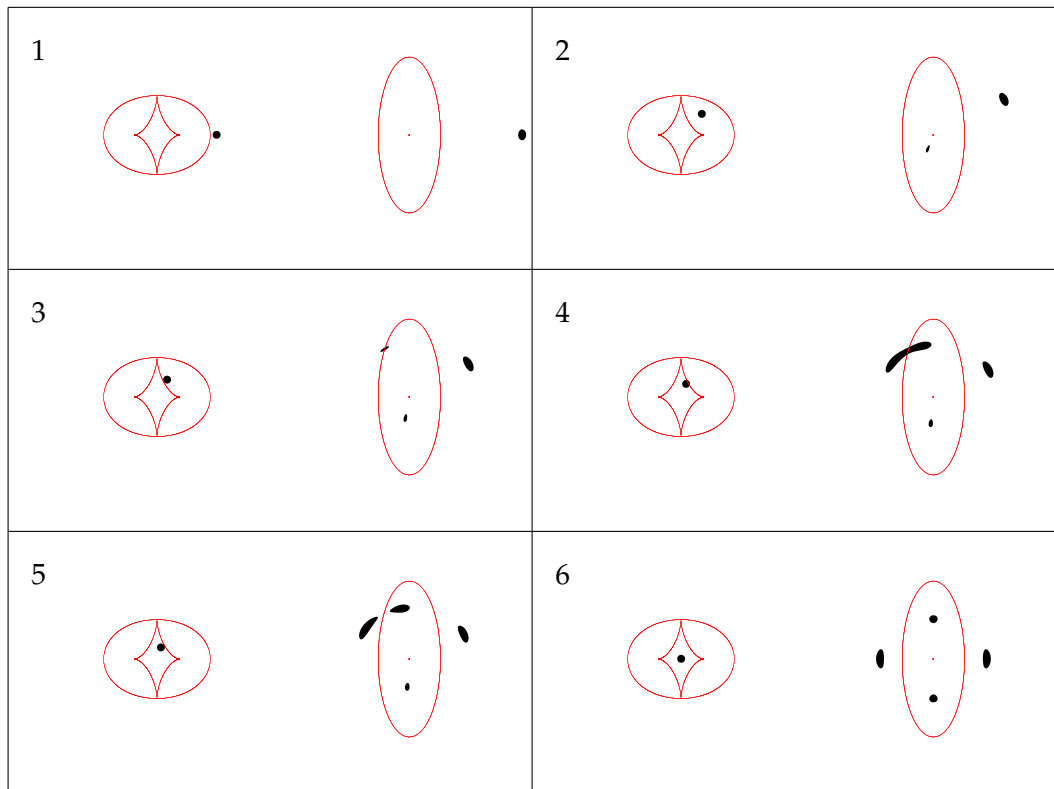


Figure 2.6: The images that are gravitationally lensed by an elliptical mass distribution. Each panel shows the source plane on the left, displaying the position of the source (black) and the caustics of the lens (red). Similarly the right side of each panel shows the images (black) and critical lines (red) in the image plane.

where f is a measure for the ellipticity (chosen to be 0.4 in the example above) and x_c is the core radius. Isothermal means that the galaxy consists of a self-gravitating spherical distribution of stars (similar to a self-gravitating sphere of a hydrostatic gas) and so the distribution is proportional to $\frac{1}{|\theta|}$. The parameter x_c removes the singularity from the distribution at the origin, hence the name non-singular. The singularity would otherwise result in an error during the numerical calculation. Still, in the examples given above the core radius was set to a very small value (10^{-8}). This makes the distributions nearly singular and so the radial critical line practically becomes a degenerate point at the origin. Due to this degenerate point only one extra image appears, as opposed to two extra images in a normal situation, when the source moves across the radial caustic. In a normal situation the radial critical line would have some extent and then this third image would appear inside this critical line.

The last example of the elliptical distribution showed that the caustics define different regions in which a certain number of images can be expected, given that the source is situated inside those regions. If a source is located outside all caustics, then only one image can be expected. When the source crosses one caustic (whichever one it is) towards the centre of the lens, then two extra images appear. As already stated only one image emerges in case of a singularity in the distribution. Finally, if the source moves across a second caustic towards the centre, then five (or four, if a singularity is present) images will be produced.

So in general it can be said that when a source crosses a critical line, two extra images will be formed. This can be translated to a rough criterion for which multiple images are likely to occur. Recalling the amplification matrix eigenvalues $\lambda_t = 1 - \kappa - \gamma$ and $\lambda_r = 1 - \kappa + \gamma$, it follows that the condition $\kappa_{max} > 1$ must hold for multiple images to occur, as the shear is small near a peak in the convergence.

3

Calculation aspects

With the theory of gravitational lensing explained in the previous chapter, now the theory can be applied to simulated galaxy clusters. After calculation of the lensing properties, these properties can be characterized for each of the clusters. The simulated galaxy clusters and other input for the computations are discussed in the first section. In the next section some details are given of the implementation of the theory. The final section outlines which computational results can be used to quantify the lens properties.

3.1 Input

Galaxy clusters — Galaxy clusters are the objects of which the gravitational lensing properties have to be determined. These clusters are the main input for the calculations discussed in this report. They are simulations done by GADGET¹. GADGET is a program specialized to cosmological N -body simulations. (Also smoothed particle hydrodynamics can be included, but that was not needed for the simulation of the galaxy clusters.) GADGET computes gravitational forces with a hierarchical tree algorithm. GADGET follows the evolution of a self-gravitating collisionless N -body system.

Two simulations were used in the calculations of this report. The first is a CDM cosmology simulation, whereas the second one contains WDM with a WDM particle mass of $0.5 \text{ keV} / c^2$. The simulated clusters used for this report consist of millions of point masses contained in a cube with sides of 150 Mpc, representing a total mass of more than $2 \cdot 10^{17} M_{\odot}$. See table 3.1 for more details of the two simulations.

From the box simulated by GADGET, first the heaviest galaxy cluster has to be found. This is done by projecting the mass onto two (perpendicular) planes, for example the xy - and yz -plane. The result consists of two (two-dimensional) grids, each of which having a bin with a maximum value for the projected mass. The coordinates corresponding to this

¹<http://www.mpa-garching.mpg.de/gadget/>

	quantity	units	CDM	WDM
	energy DM particle	[keV/ c^2]	–	0.5
simulation	mass	[$10^{15} M_\odot$]	270	280
	side length box	[Mpc]	150	150
	density	[H atom/cm ³]	1.6	1.7
	particles	[10^5]	42	110
cluster	mass	[$10^{15} M_\odot$]	1.1	1.4
	radius selection	[Mpc]	5	5
	particles	[10^5]	7.8	9.5
	Einstein radius θ_E	[Mpc] [arcsec]	0.38 1.5	0.43 1.7
central region	mass	[$10^{15} M_\odot$]	0.14	0.17
	radius selection	[Mpc]	0.31	0.31
	particles	[10^5]	0.90	1.12

Table 3.1: Specifications of the simulated galaxy clusters. The whole simulation is a box, but the cluster and the central region are selected to be concentric spheres. The cluster is defined by a radius of 5 Mpc and the central region is defined by $1/2^4$ of the radius of the whole cluster. The distances used for the Einstein radius are given in section 3.1.

bin will be used as the centre of the cluster of interest. A selection is made of all particles that are located within a distance of 5 Mpc around the centre. The cluster is then rotated into an arbitrary orientation (see appendix A.1) before being projected on a final grid. The reason for this random rotation will be explained in section 3.3. The projection results in a square matrix with sides of N elements, where each element is the sum of the mass along the line-of-sight. After division by the area of one pixel the matrix represents the surface mass density. The choice of N sets the resolution of the whole calculation, because the matrices featuring in the rest of the calculations will have the same size. Eventually the results will be presented as images, where each pixel is one element of the matrix.

Besides the mass distribution, there is another input of the calculations, namely the angular-diameter distances D between the observer, lens and source plane. These distances are important for the occurrence and strength of the lensing effects. When defining the position of the objects by a certain red shift, then the distances can be calculated, if a particular cosmology is given. This is done with the use of the formulas given in [6] which assumes a homogeneous Friedmann-Lemaître cosmology (the “standard” Λ -CDM cosmology model), parametrized only by the Hubble constant H_0 , cosmological constant Λ and the density parameter $\Omega_0 = \frac{8\pi G\rho}{3H_0^2}$ where ρ is the matter density of the universe. In all calculations the lens is put at a red shift of $z_l = 0.3$ and the source at $z_s = 2.0$. When assuming that the cosmology parameters are set to $H_0 = 72$ km/s/Mpc and $\Omega_0 = 0.27$, then the angular-diameter distances are given by $D_l = 900$ Mpc, $D_s = 1725$ Mpc and $D_{ls} = 1335$ Mpc.

With the angular-diameter distances specified, the critical surface mass density (formula 2.7) can now be calculated, as it does not depend on other variables. So the critical surface mass density for both the CDM and WDM cluster is given by $5.0 \text{ kg/m}^2 = 2.4 \cdot 10^9 M_\odot/\text{kpc}^2$, respectively. Dividing the surface mass density of the cluster by the critical density, results in the convergence (formula (2.8)). This is already a main property in gravitational lensing and now all calculations explained in the previous chapter can be done.

Smooth mass distribution — The convergence effectively still consists of point (or now actually pixel) sources due to the way of simulation by GADGET. In order to get a realistic convergence, smoothing has to be applied. This is done by convolving the convergence with a two-dimensional circular Gaussian distribution. This (normalized) Gaussian distribution is given by

$$G(\vec{\theta}) = \frac{1}{2\pi\sigma^2} e^{-\frac{|\vec{\theta}|^2}{2\sigma^2}}, \quad (3.1)$$

where σ is the standard deviation of the Gaussian. A realistic map for the convergence is found by convoluting it with this Gaussian.

The smoothing is characterized only by σ , which is a characteristic length called the smoothing radius. This radius was chosen to be 5 kpc because of a reason explained in the next section.

3.2 Implementation

The calculation of the lensing properties explained in the previous chapter are fairly straightforward. As the convergence is given by a matrix and not by a well defined function, the actual calculations are done numerically. The program MATLAB is used to do these calculations. The program already has the built-in functions `fft2` and `ifft2` which perform the two-dimensional Fourier transformation and its inverse, respectively, on a matrix. In turn, these algorithms use the discrete Fourier transform. In this section some details and issues of the calculation are highlighted as they are important steps in getting the final results.

Zero padding and shifting — There are a considerable amount of convolutions to be calculated. As shown at the end of section 2.1 a convolution is equivalent with a multiplication in Fourier space. A little bit of attention is needed on how this is done exactly.

The calculations involve the convolution of the convergence, denoted by f for now, with some kernel g . For simplicity only a one-dimensional distribution will be considered, but the same reasoning holds for two dimensions. It will be assumed that both distributions have the same length of N values. As example a Gaussian f is considered in combination with a constant kernel g . This situation is shown in the left column of

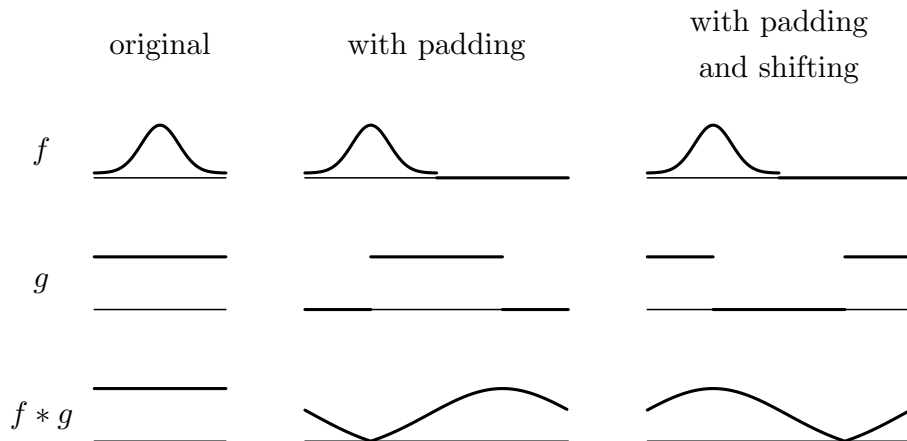


Figure 3.1: The effect of zero padding and shifting of the functions in a convolution. A more detailed description is given in the text.

figure 3.1, which also includes the result of the convolution $f * g$. This result does not look like a Gaussian any more. The reason for this is that by using Fourier transforms, periodicity of the functions is assumed. This can be explained by the formula for circular convolution given by

$$(f * g)[i] = \sum_j f[j]g[i - j + 1], \quad (3.2)$$

where $i, j = 1, 2, \dots, N$ are the indices as the functions f and g are represented by vectors. The combination $i = 3, j = 7$ and $N = 11$ would result in $g[i - j + 1] = g[-3] = g[8]$, because of the periodicity.

A method to get around this periodicity is adding N zeros to the function f (as explained in [7]). The convolution remains the same, as it is defined (in this example) as 1 over a length of N around the centre of the kernel. The zero padded function, the extended kernel and the convolution of the two functions are depicted in the middle column of figure 3.1. Due to the padding, the convolution is effectively linear and not circular any more. This means that there are no periodic effects any more and so the convoluted function is Gaussian again.

A side effect of doubling the length of the functions is that the resulting convoluted function will also be doubled in length. The original, first half of the convoluted function should be selected as the actual result. As can be seen in the middle column from figure 3.1, the selected part (first half) would not be the wanted result. Therefore the kernel can be shifted by N (to either side, as the function has length $2N$) in order to automatically select the correct part as result. The right column in the figure shows this final, correct method to do the convolution of two functions.

The actual calculations involve the convolution of two-dimensional matrices. The padding and shifting should be applied in both directions by

$$F \xrightarrow{\text{padding}} \begin{pmatrix} F & 0 \\ 0 & 0 \end{pmatrix} \quad \text{and} \quad \begin{pmatrix} G_{11} & G_{12} \\ G_{21} & G_{22} \end{pmatrix} \xrightarrow{\text{shifting}} \begin{pmatrix} G_{22} & G_{21} \\ G_{12} & G_{11} \end{pmatrix}. \quad (3.3)$$

Note that the multiplication of the Fourier transformed matrices is not a matrix multiplication and should be done element-wise.

Singularities — When stating the convolution kernels, used to calculate the deflection angle and amplification matrix (formulas (2.22) and (2.23)), no attention was paid to the fact that they contain a singularity at the origin $\vec{\theta} = (0, 0)$. In order to represent the kernels as a matrix in the numerical approach, the pixel at the origin should be defined by a finite value. However, it is not clear what this value should be as the limits of the kernels go to $\pm\infty$.

When considering the central pixel of the kernel only (value denoted by C), then the value of the centre of the convoluted matrix is given by

$$\frac{1}{\pi} \int \kappa(\vec{\theta}') C \delta^{(2)}(\vec{0} - \vec{\theta}') d^2\vec{\theta}' = \frac{C}{\pi} \kappa(\vec{0}) A_{pix} = \begin{cases} \kappa(\vec{0}) & \text{if } C = \frac{\pi}{A_{pix}} \\ 0 & \text{if } C = 0 \end{cases}$$

where A_{pix} is the area of one pixel. From this it can be concluded that the central pixel of the kernel is responsible for the convergence. It also represents the mass inside the bundle of photons (that goes through the lens at this position). Subsequently, the rest of the kernel incorporates the dependence on the mass outside of the bundle and results in the deflection angle/shear (depending on the kernel). For this reason the central value for the deflection angle kernels have to be zero, because no convergence should be included in the result. In case of the amplification matrix

$$\begin{aligned} \psi_{11} &= \kappa + \gamma_1 \\ \psi_{12} &= \gamma_2 \\ \psi_{22} &= \kappa - \gamma_1 \end{aligned}, \quad (2.15)$$

so the central pixels should be $\frac{\pi}{A_{pix}}$ for the kernels for calculating ψ_{11} and ψ_{22} and zero when dealing with the kernel for ψ_{12} . If all central values would be zero, then the convolution only returns the shear and not the convergence.

Inner and outer region — The resolution of the simulation is determined by the size of the matrix and is a measure of how detailed the analysis will be done. The central part of the calculated region has the biggest lensing effects because of its high convergence. In order to be able to do a detailed analysis of the lensing properties, a more detailed calculation of this central region will be done.

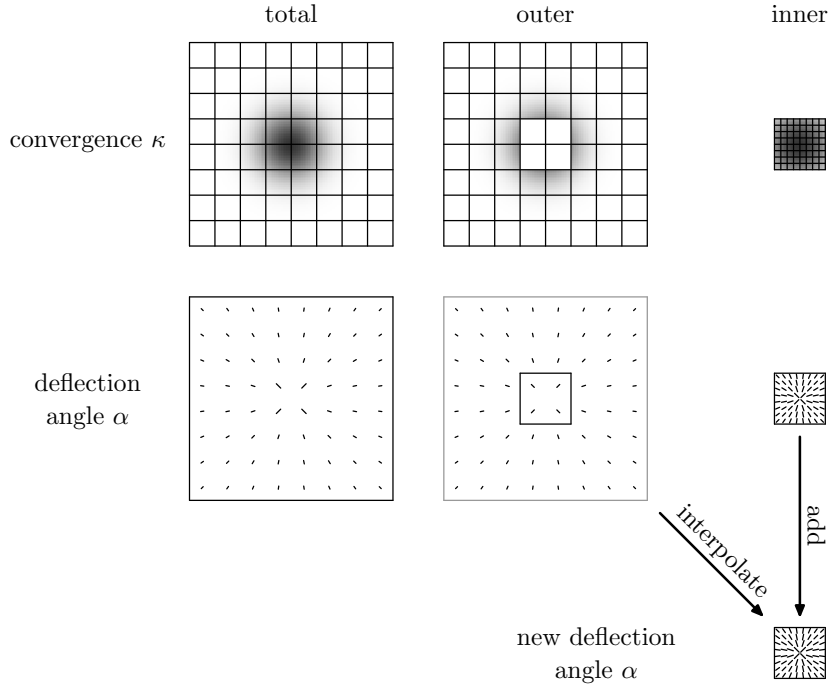


Figure 3.2: The steps needed for a detailed calculation of the complete and inner region. The calculation of the outer region is interpolated and added to the calculation of the inner region, in order to incorporate the effects of the mass in the outer region in the result of the inner region. See text for more details.

At first sight it seems that, besides a calculation using the convergence of the whole region, only one extra calculation is needed for the central region. This is not true. The calculation needs to be done for three regions, the complete, the inner, but also the outer region. See the top row of images in figure 3.2. To explain this, one needs to recall that the shear is affected by the mass located around the point of interest. This means that if the inner region is calculated on its own, then it does not incorporate the mass in the outer region. The same holds for the deflection angle. The schematic diagram in figure 3.2 shows how the deflection angle calculation for the outer region is used to get an accurate description of the inner region. The influence of the outer region is included by interpolating and then adding it to the inner region calculation. For shear the same has to be done as for the deflection angle. This method is also used in [8].

The cluster contained in the complete region is defined by a radius of 5 Mpc. The detailed inner region has a radius 2^4 times smaller, about 0.31 Mpc. All matrices used in the calculations have size $N \times N$. So, incorporating the angular-diameter distances D , the resolution for both regions is determined and given in table 3.2.

units	[10^{-6} rad]	[arcsec]	lens plane [kpc]	source plane [kpc]
outer region	10.9	2.24	9.77	18.7
inner region	0.678	0.140	0.610	1.17

Table 3.2: The resolution of the calculation of the outer and inner region.

With the calculations of both inner and outer region, a condition can be defined for the amount of smoothing. For a smaller smoothing radius (less smoothing), the maximum convergence of the total region would remain the same, but for the inner region the convergence would increase. If the smoothing radius would be larger (more smoothing), then for both regions the maximum convergence would start to drop as the mass gets smeared out over space. As mentioned in the previous section the smoothing radius is chosen to be 5 kpc. In this case the maximum convergence for the inner and total region differ least and they do not start to drop.

Solving lens equation, making images — As derived in the previous chapter, the lens equation is given by

$$\vec{\beta} = \vec{\theta} - \vec{\alpha}(\vec{\theta}) . \quad (2.6)$$

It is important to note two aspects of this equation. Firstly, the deflection angle $\vec{\alpha}$ depends on the coordinate in the lens plane $\vec{\theta}$ and, secondly, the equation holds in both x - and y -direction. In other words, $\vec{\alpha}$ is represented by two matrices, one for each direction. Each element corresponds to a certain position $\vec{\theta}$. Also $\vec{\theta}$ consists of two matrices and so does $\vec{\beta}$. The coordinates of $\vec{\theta}$ are defined by the coordinates of a straight grid. After subtraction of the deflection angle, the result consists of the two matrices with the coordinates of $\vec{\beta}$, so an observed light ray coming from direction $\vec{\theta}_{ij}$ is actually coming from the angle $\vec{\beta}_{ij}$.

Now it is important to understand how this representation of the coordinates can be used. A source and its images will be depicted by a binary matrix, so with only zeros and ones. The matrix with the images I corresponding to a uniform circular source, with radius r_s and origin at position (x_s, y_s) , is given by

$$I = \begin{cases} 1 & \text{if } (\beta_x - x_s)^2 + (\beta_y - y_s)^2 \leq (r_s)^2 \\ 0 & \text{otherwise} \end{cases} .$$

The reason why this equation gives the images is because some element I_{ij} (at position $\vec{\theta}_{ij}$) is true (part of an image) if its coordinate $\vec{\beta}_{ij}$ in the source plane is contained within the source circle. In order to picture an unlensed source, the deflection can be taken to be zero and then $\vec{\beta} = \vec{\theta}$. So then the circular source is depicted by matrix S , given by

$$S = \begin{cases} 1 & \text{if } (\theta_x - x_s)^2 + (\theta_y - y_s)^2 \leq (r_s)^2 \\ 0 & \text{otherwise} \end{cases} .$$

This is because pixel S_{ij} is part of the source if the coordinate $\vec{\theta}_{ij}$ (part of straight grid) is enclosed by the circle describing the source. Of course, also other types of sources can be used. For example, a two-dimensional Gaussian with its centre at (x_s, y_s) and a standard deviation of r_s results in images given by

$$I = \frac{1}{2\pi r_s^2} e^{-\frac{(\beta_x - x_s)^2 + (\beta_y - y_s)^2}{2r_s^2}}.$$

3.3 Getting results

After knowing the theory and the details of the calculation, now more attention can be paid to what actual analysis can be done. The question is what the interesting quantities are for being able to say something about the differences in gravitational lensing properties of the CDM and WDM galaxy clusters. Two different kinds of analysis will be looked at, which characterize the properties of the lens itself and the gravitational lensing properties. These will be explained in this section.

Properties of the lens — A first point of detail is that the calculation starts with the galaxy clusters, which are three-dimensional distributions. When the distribution is projected, then a certain line-of-sight is assumed. The lens properties and the gravitational lensing properties of the cluster can change a lot between different lines-of-sight. This is the reason why each cluster is rotated multiple times in order to get a distribution of a certain property for that cluster. So now the question is what properties are useful to keep track of when doing the calculations for different rotations of a cluster. Some properties are listed below. They are all determined using the calculation of the inner region.

- The maximum value for the convergence, κ_{max} .
- The ellipticity of the convergence map, e .
- The area enclosed by
 - the tangential caustic, A_t ,
 - the radial caustic, A_r ,
 - all caustics, A_{tot} .
- The (theoretical) area in the source plane that results in 5 (or more) images, which is the overlap between the tangential and radial caustic, $A_5 = A_t + A_r - A_{tot}$.
- The (theoretical) area in the source plane that results in 3 images, $A_3 = A_{tot} - A_5$.

Except for κ_{max} , A_5 and A_3 , the listed quantities are not calculated in a straightforward manner. Firstly, the ellipticity of an ellipse with semimajor axis a and semiminor

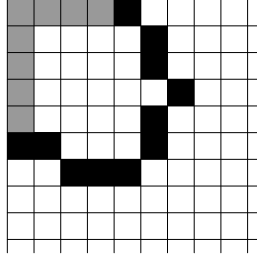


Figure 3.3: Example of a caustic (black pixels) that is an open curve, as it crosses the border of the matrix. This would result in an incorrect area calculation, unless the curve is closed along the border by adding pixels (in grey) to the curve.

axis b is defined by

$$e = \frac{a - b}{a + b}.$$

The problem is that the ellipticity can not be fit to a well-defined curve or some points, but it has to be calculated from the two-dimensional convergence map. From the many possible calculations, two methods are investigated. The first method fits ellipses to the contours of equal convergence. Another method makes use of the second moments of the distribution. This second moment method is explained in full detail in appendix A.2. Both methods yield rather different results, but the latter one is chosen as the method for this report. This choice is made, because it is the most solid one as it depends on the least number of parameters. Moreover, the method is also meant for calculating the ellipticity from a given distribution.

The next quantity on the list of interesting properties is the area of the caustics, which is well defined. The caustics are given by the coordinates β that correspond to the coordinates θ for which the eigenvalues of the amplification matrix λ vanish. This can easily be calculated by using

$$C_{ij} = \begin{cases} 1 & \text{if } S_{ij}(S_{i-1,j} + S_{i,j-1} + S_{i+1,j} + S_{i,j+1}) < 4 \\ 0 & \text{otherwise} \end{cases},$$

where $S_{ij} = \text{sign}(\lambda_{ij})$ (method from [9]). The matrix element C_{ij} is true (one) when one of the λ 's changes sign across position (i, j) in both directions. The matrix C depicts the critical lines in the lensing problem. The caustics can be constructed from the positions $\vec{\beta}_{ij}$ for which the pairs of (i, j) have $C_{ij} = 1$. By projection of these caustic points on a straight grid, a matrix can be made which contains the caustics (analogously to the matrix C). Then the area within the caustics can be filled up using the MATLAB function `imfill` with the option `'holes'`. Consequently the area within the caustics can easily be calculated by counting the number of pixels.

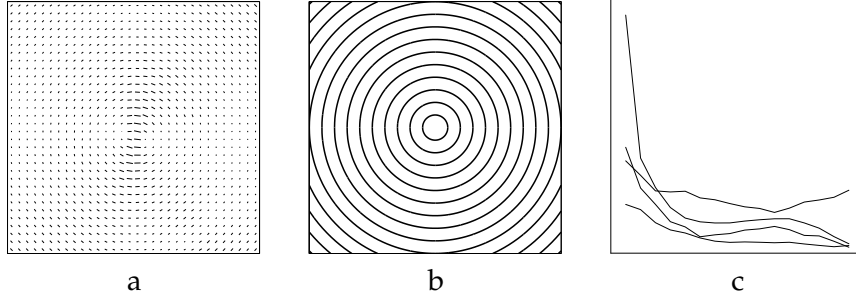


Figure 3.4: Steps in characterizing the shear map into the four quantities $\bar{\gamma}$, σ_γ , $\bar{\phi}$ and σ_ϕ . a) Some shear map calculated from the convergence. b) Map partitioned into concentric annuli. c) Plot of each quantity as a function of the radius of the annulus. The resulting parameters for each quantity are found after averaging over all points of the plot in c. More details can be found in the text.

Although the method described above is very accurate, there is a complication. In order to let the function `imfill` work, the caustics need to be closed curves after the projection. This is not the case in two situations. Firstly, the caustic can be at the border of the matrix resulting in a curve with two end points at the border. This problem can be solved by closing the curve along the border, as an example shows in figure 3.3. Secondly, there are situations when too few points describe a segment of the caustic, which results in gaps in the curve. In practice it appears that these gaps are not wider than two pixels. For this reason algorithm `FillGaps` is created to close these gaps. This algorithm first searches for all the endpoints of the lines. Then each endpoint is connected to the nearest neighbouring pixel, within a distance of two pixels and that is not connected to the endpoint. A more detailed description of this method can be found in appendix A.3.

The last quantity, which can be observed almost directly, but is not mentioned in this section yet, is the shear. As explained in section 2.2 the shear can be represented by the two components γ_1 and γ_2 , but also by the amplitude $\gamma = \sqrt{\gamma_1^2 + \gamma_2^2}$ and the direction $\phi' = \frac{1}{2} \arctan \frac{\gamma_1}{\gamma_2}$ (previously referred to as ϕ). Using the vector representation of the shear, a shear map can be made. In such a map the shear is depicted by "compass needles" (headless arrows) of length γ and direction ϕ' as shown in figure 3.4a.

One shear map contains so much information that it is hard to characterize it in just a couple of numbers. In an attempt to do so, first the map is divided into a series of concentric annuli as shown in figure 3.4b. For each annulus the properties γ and ϕ for points inside that annulus are selected, where ϕ is ϕ' subtracted with the angle of the tangent of the annulus (the reason for this follows). Then the selected values of γ and ϕ are used to calculate the properties

- $\bar{\gamma}$: the average of the amplitude γ ,
- σ_γ : the standard deviation of the amplitude γ ,

- $\bar{\phi}$: the average of the angle ϕ , and
- σ_{ϕ} : the standard deviation of the angle ϕ .

These four quantities are calculated for each annulus and so they can be presented as a function of the radius of that annulus, as depicted in figure 3.4c. Finally, in order to get only one value per orientation of the cluster, each quantity is averaged over all annuli. Of course, all these quantities can be calculated for both the outer (subscript o) and inner (subscript i) region. So this leads to eight quantities, denoted by $\bar{\gamma}_o$, σ_{γ_o} , $\bar{\phi}_o$, σ_{ϕ_o} , $\bar{\gamma}_i$, σ_{γ_i} , $\bar{\phi}_i$ and σ_{ϕ_i} , as an attempt to characterize the shear for one rotation.

The reason why the tangent of the annulus is subtracted from the direction of the shear is because this value could be expected in an idealized case. A lens consisting of a circularly symmetric mass distribution that decreases with distance from the centre (as expected), would result in a circularly symmetric shear map. In this case the direction in each point would follow the tangent of a circle. That is why this expectation value is subtracted from the calculated value. This means that when the analysis returns $\bar{\phi} = 0$ and $\sigma_{\phi} = 0$, then this will indicate that the lens is perfectly circular. The greater their values, the more the lens deviates from this symmetrical case.

Properties of lensing effects — Besides the properties of the lens for a certain rotation, another way of characterizing the gravitational lensing properties of a cluster is to look at the images it produces. The quantities that matter in this, are the number of images produced and the total magnification of the source.

The calculated magnification is not used for characterization of the gravitational lensing properties. This is because the magnification can become very high, approaching infinity. This is due to the fact that the calculation assumes infinitesimally small sources at the grid points and so the magnification could in principle be infinite. Of course, this result is not realistic, because in reality sources are extended (consisting of multiple pixels). For extended sources, the magnification could be approximated by averaging the magnification over the area covered by the source (weighted by the surface brightness). But another way of calculating the magnification is dividing the area of the images by the area of the source. This method is used in this report.

In order to quantify what the gravitational lensing properties are for a certain cluster orientation, a source can be put in the source plane and consequently the images can be inspected. By using a lot of sources, all the magnifications of the images can be used to make a distribution of the probability to get a certain magnification of one source.

So, for this report, when making a magnification probability distribution for a certain cluster orientation, 300.000 uniform circular sources are placed randomly in the source plane of which 100.000 are put in the outer region and 200.000 in the inner region. The reason to position the sources randomly (instead of on a grid) is to prevent introduction of any systematic errors. To identify all images in a binary matrix, a method had to be

defined. In appendix A.4 this algorithm is explained in full detail. Subsequently the number of images and their combined magnification is calculated and so a magnification probability distribution can be made.

The just mentioned steps are pretty straightforward, except for one aspect. When producing the magnification probability distribution it has to be incorporated that results come from calculations of both the outer (area A_o) and inner region (area A_i). The results for the probability distribution of both the outer (P_o) and inner region (P_i) need to be combined in a total distribution. This total distribution is calculated for the whole sky and it includes the separate distributions in the following manner

$$P(\mu) = \frac{A_r P_r(\mu) + A_o P_o(\mu) + A_i P_i(\mu)}{4\pi},$$

where $A_r = 4\pi - A_o - A_i$, which is the area of the rest of the sky excluding the lens. Note that the areas are actually solid angles and so the whole sky covers 4π . The distribution for the rest of the sky is not calculated, but just given by the function $P_r(\mu) = \delta(\mu - 1)$. This assumes that no gravitational lensing effect occurs outside the lens and so the magnification is one. Moreover the distribution will peak around $\mu = 1$, because both A_o and A_i are very small compared to A_r .

3.4 Expected results

After all quantities to characterize the lens and its gravitational signature are defined and treated, now it is time to think about what results could be expected.

Properties of the lens — Of course, the main question is if a CDM and a WDM cluster can be identified from the observation of their gravitational properties. As explained in chapter 1, during structure formation dark matter plays an important role as it makes up 27% of the universe's energy content. The type of dark matter results in more subtle features. Where clusters in a CDM cosmology universe can become very massive, WDM would result in more, but less heavy cores in single clusters. So, this means that WDM clusters will have more structure. This can effect the correlations between quantities.

First, an example is considered to illustrate the relation between the maximum convergence and the ellipticity. Assume a mass distribution shaped like an ellipsoid with semi-principal axes a , b and b where $a > b$. When the semi-principal axis of size a is aligned with the line-of-sight, then the highest κ_{max} can be expected. Another feature is that the ellipticity will be zero as the two perpendicular axes are equal. Conversely when a semi-principal axis of size b would be along the line-of-sight, then the ellipticity would not be zero and the convergence would decrease. So in case of an ellipsoid an inverse correlation between κ_{max} and e can be expected to emerge.

This example distribution, shaped like an ellipsoid, could also be a probable scenario for a cluster used in this report. They originate from a simulation in which the matter collapsed into clusters and so it will be very unlikely for the mass distribution to be perfectly spherical. Another aspect in relating κ_{max} and e is the amount of structure of the cluster. As the CDM cluster will have one main structure, the correlation could be clearly visible. But in the case of the WDM cluster, one could expect less correlation as more structure could be present in the cluster.

When considering the tangential caustic, it will be useful to recall the examples of caustics discussed in section 2.2. When the convergence map is very circular, then the tangential caustic will cover only a small area. Conversely, a high-ellipticity distribution will result in a bigger tangential caustic. From this it can be concluded that a positive correlation between the ellipticity and tangential caustic area can be expected. Similarly the radial caustic is linked to the convergence, because a high convergence will lead to a bigger radial caustic. So also a positive correlation can be expected between κ_{max} and A_r . When comparing the CDM and WDM cluster, more spread will be expected for the WDM cluster, as its structure will result in a larger range of possible values.

Of course, there will be a clear relation for the areas corresponding to 5 and 3 images, as the relations are given by definition,

$$A_5 = A_t + A_r - A_{tot} \quad \text{and} \quad A_3 = A_{tot} - A_5 .$$

In case of correlation in A_t , A_r and A_{tot} as a function of κ_{max} or e , then these will also emerge in the plots relating A_5 and A_3 with κ_{max} or e . The area in which sources will result in 5 (or more) images is the area where the tangential and radial caustic overlap. The remaining part of the caustic is denoted by A_3 . The total area is given by

$$A_{tot} = A_5 + A_3 \approx A_t + A_r ,$$

where the last approximation holds only when A_5 is small compared to the other areas A_t and A_r .

Lastly, it would be interesting to find a relation between the shear and some other property. The most promising candidate would be the ellipticity, because a shear map shapes itself around the convergence. As already explained in the previous section, especially the quantities $\bar{\phi}$ (average of angle ϕ) and σ_ϕ (standard deviation of angle ϕ) are interesting, as they will be zero, when the ellipticity is also zero. So perhaps a positive relation can be recognized between $\bar{\phi}$ and/or σ_ϕ and the ellipticity e .

Considering the shear in general, then a lot of structure (as in the WDM cluster) would result in high values for all quantities $\bar{\gamma}$, σ_γ , $\bar{\phi}$ and σ_ϕ . They are calculated for both outer and inner region. It could be that the outer region is very noisy, whereas the inner region contains only a part of the cluster and so the correlations are clearer for the inner region.

Properties of lensing effects — To conclude this section, the probability distribution of the source magnifications will be investigated. There are a few features that can occur in the distribution which are already reported in the past. What causes underlie these effects, will be treated in the following.

In [4] an approximate derivation is done for the general behaviour of the high-magnification tail of the distribution. This tail is dominated by sources close to the caustics. As mentioned before, these sources will result in two big images and other smaller images, which will not be of interest here. The derivation starts with the situation in which a point source is considered and a lens, which has a critical line $\vec{\theta}_c(t)$, where t is some parametrization coordinate. Then some point close to the critical line is taken, which is at a distance w from the closest point on the critical line $\vec{\theta}_c$. Then the magnification can be approximated by

$$\mu \approx \frac{1}{|\nabla \det A(\vec{\theta}_c)| w},$$

where the term $|\nabla \det A(\vec{\theta}_c(t))|$ is the gradient of $\det A$ at the critical line, so it will be perpendicular to the critical line. This can be used to calculate the area on one side of the closed critical line where the magnification is larger than μ , which is

$$a(\mu) \approx \oint dl w = \oint dt \frac{dl}{dt} \frac{1}{|\nabla \det A(\vec{\theta}_c)| \mu} = \frac{C}{\mu},$$

where dl is a line segment of the critical line and so the integral runs over the whole critical line and C is some constant. With this, the area in the image plane with magnifications between μ and $\mu + d\mu$ is

$$\left| \frac{da(\mu)}{d\mu} \right| d\mu = \frac{C}{\mu^2} d\mu.$$

Now a similar area in the source plane (where the magnification lies between μ and $\mu + d\mu$) can be calculated by including the magnification factor as $\frac{1}{\mu}$

$$\left| \frac{d\sigma(\mu)}{d\mu} \right| d\mu = \frac{1}{\mu} \left| \frac{da(\mu)}{d\mu} \right| d\mu = \frac{C}{\mu^3} d\mu.$$

Integrating this will result in the area in the source plane, for a magnification $> \mu$, of

$$\sigma(\mu) = \frac{C}{2\mu^2}. \quad (3.4)$$

Finally the high-magnification behaviour of the image magnification probability distribution can be calculated and is given by

$$P(\mu) \propto \left| \frac{d\sigma(\mu)}{d\mu} \right| \propto \mu^{-3}. \quad (3.5)$$

Note that so far only the source magnification probability distribution was mentioned, which is different from the image magnification probability distribution. In this report the total magnification of a source is of interest, not the magnification of all individual images. The derivation is based upon the fact that the source results in two big images with magnification $> \mu$. This means that the magnification of the source is roughly twice the image magnification μ and so the proportionality of the source magnification probability distribution is still μ^{-3} . An exact derivation is also done in [4] and originally in [10]. Note that this proportionality is derived for the case of point sources magnified by single lenses with an arbitrary mass distribution. In other situations, this proportionality of μ^{-3} does not need to hold and a more detailed analysis is needed in those cases. Still, the articles [11] and [12] found that their results obeyed this behaviour.

There are two aspects in the previous derivation which can change the behaviour of the high-magnification tail of the probability distribution. Those aspects are the ellipticity of the lens and the finite-size of the sources. Those are both considered in [11]. Firstly, although the derived power law of μ^{-3} should be applicable to every arbitrary mass distribution, the ellipticity of the lens changes this general behaviour. The ellipticity leads to bigger caustics, so a larger region in which sources get highly magnified. That is why ellipticity of the lens results in higher magnifications.

Secondly, also extended sources influence the tail of the distribution. In both [4] and [11] finite-sized sources are considered and they show that the tail will rapidly decrease after some cut-off magnification. The reason for this is that the magnification of an extended source is more averaged as it covers a bigger area. Consider a small source on a caustic. If the source would be infinitesimally small, then the magnification would be infinite. But the bigger the source would be, the lower the average magnification becomes. This effect is even bigger when the lens is more elliptical. The caustic of an elliptical lens becomes larger, but also narrower and so the influence of the source size will be even greater. The relevant factor in this is the ratio of the source size to the Einstein radius θ_E . In [11] the ellipticity was ranged from 0.1 to 0.4 and the source sizes were $0.023\theta_E$ and $0.041\theta_E$. The resulting maximum magnification shown lies between $\mu \approx 50$ ($e = 0.4$ and source size of $0.041\theta_E$) and $\mu \approx 100$ ($e = 0.1$ and source size of $0.023\theta_E$).

There is another feature that can be present in the magnification probability distribution around intermediate magnifications. In [12] the "second bump" around $\mu \approx 5$ (in comparison to the first peak at $\mu = 1$) is investigated. For this purpose the probability distribution is split up into the distribution corresponding to the magnifications in case of one, three, five, ... images. This showed that the distribution for one image is a nicely decreasing curve following a power law with an exponent < -3 . The distribution of three images becomes the main component of the distribution around $\mu \approx 5$, creating a bump. After that, the curve follows a power-law with exponent -3 . It was concluded that the bump was due to sources near caustics, resulting in an extra pair of big images.

4

Results

The results of the analysis described so far, are presented in this chapter. The first section shows the characterization of the properties of the lens for different rotations of the galaxy clusters. The magnification probability distribution for certain projections of the clusters will be given in section two. The chapter is concluded with a discussion of the results.

4.1 Rotations

The simulated clusters will have different gravitational lensing properties when the line-of-sight changes. In order to get a complete picture for one cluster, the properties are calculated for 5000 different random orientations. This section will investigate the maximum convergence, ellipticity, caustic areas and shear measures. Especially correlations between them would be interesting to find.

Before investigating the quantities in detail, first some general parameters of the distribution of the properties will be considered. Figure 4.1 shows an unconventional box plot with the minimum, maximum, average value and also the standard deviation for each property and cluster. One important feature is that all parameters of the WDM cluster are approximately equal or greater than the ones of the CDM cluster. Later in this chapter, a couple of references will be made to this figure. In the last section a discussion of this figure will be given.

So now all quantities will be investigated both separately as well as together in order to search for correlations.

Convergence and ellipticity — The first quantities of interest are the maximum convergence κ_{max} and the ellipticity e of the lens. The example given in section 3.4 showed that a matter distribution shaped like an ellipsoid would have an anti-correlation between κ_{max} and e . So when the convergence is high, then the ellipticity will be low and vice versa. This is exactly the case for the CDM cluster, as will be shown.

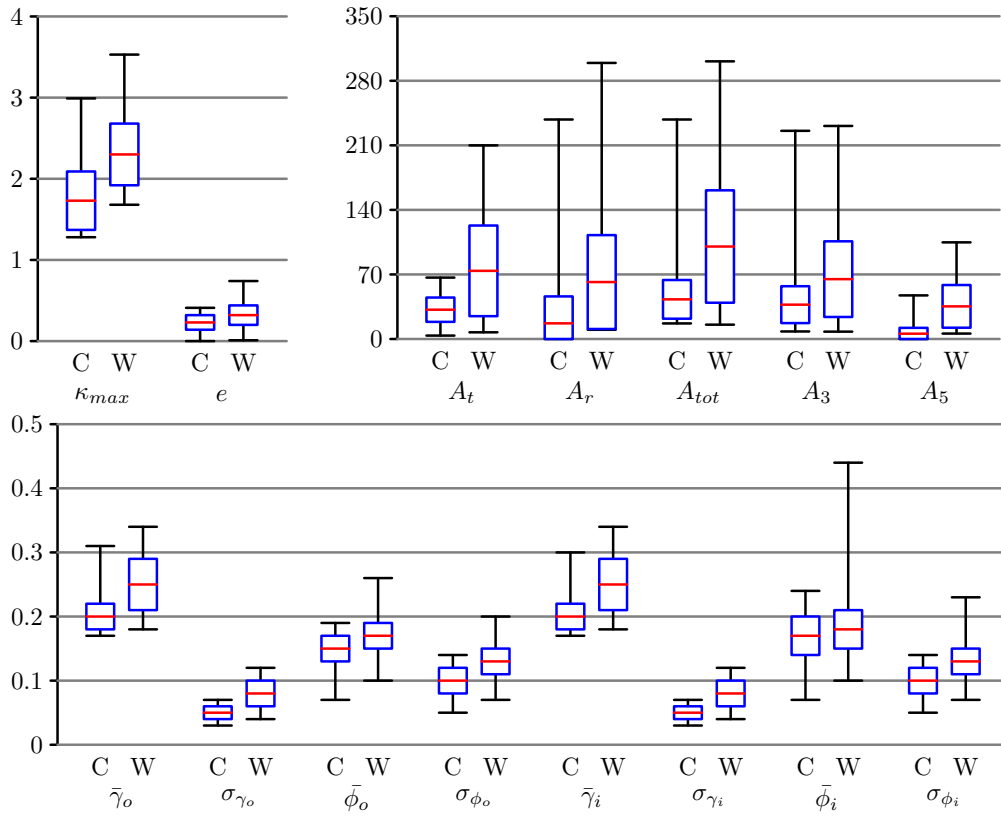


Figure 4.1: (Unconventional) box plot containing the statistical properties of all quantities of interest for both the CDM (C) and WDM cluster (W). Each box plot shows the average (red middle line), the standard deviation on both sides (blue boxes) and the extreme values (black whiskers) of each quantity.

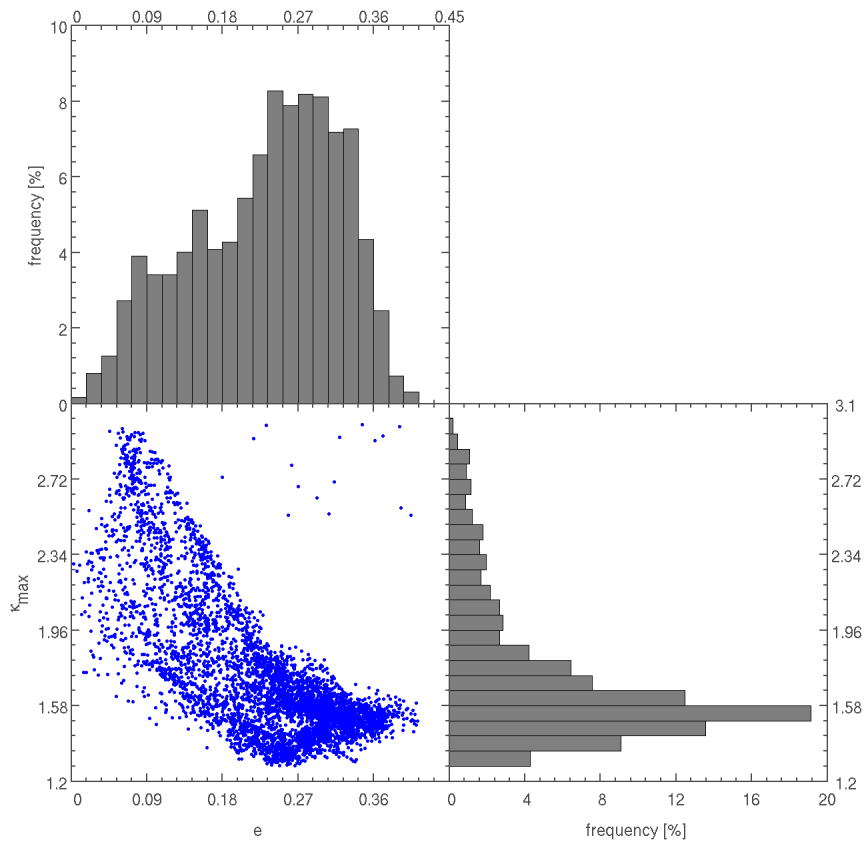


Figure 4.2: Distributions of the ellipticity (top left) and the maximum convergence (bottom right) and a plot of the convergence as a function of the ellipticity (bottom left). All results based on 5000 different rotations of the CDM cluster.

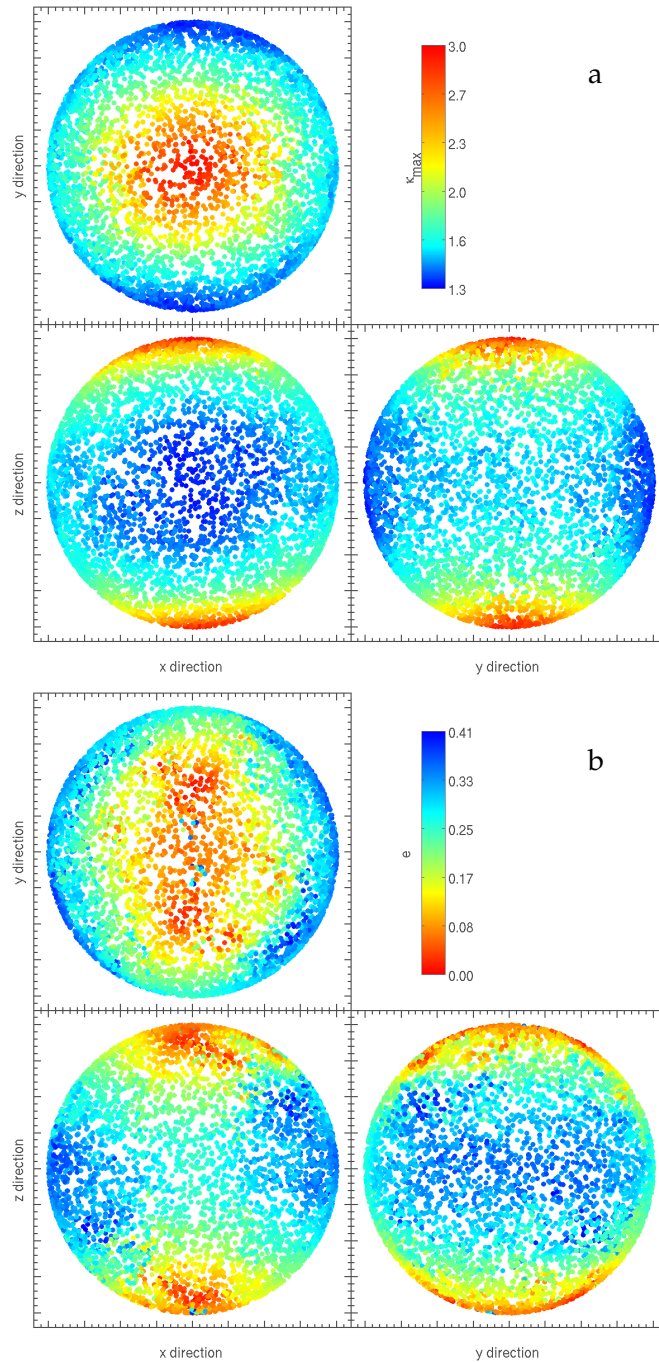


Figure 4.3: Projections of a) the maximum convergence (three top plots) and b) ellipticity (three bottom plots) as a function of the orientation of the CDM cluster. The line-of-sight of an orientation corresponds to the position of the point in that direction on a sphere with its origin in the centre of the plots. The strength of the quantities is represented by the colour of the points. Note the different colour scaling for the two quantities.

In figure 4.2 the distribution of both the maximum convergence and the ellipticity are given, but also the correlation plot. Although slightly noisy, there is a clear trend between the ellipticity and the maximum convergence that indicates an inverse correlation. As explained, this means that the CDM galaxy cluster can be described by an ellipsoid. More (detailed) evidence for this feature can be found when looking at κ_{max} and e as a function of the orientation. These spatial distributions are shown in the figure 4.3. Especially when looking at the convergence plot it becomes clear that the CDM cluster is shaped like an ellipsoid. But in this case an ellipsoid with three different semi-principal axis a , b and c where $a > b > c$. The cluster is rotated so as to align axis a with the z -axis and c with the y -axis. Note that two exactly opposite directions result in the same distribution (but flipped).

The ellipticity in figure 4.3b shows that the ellipticity is low when the convergence is high and vice versa. Because of the ellipsoidal structure, a lot of orientations result in a high ellipticity and low convergence. This is also the reason for the great amount of points in the bottom right corner of the correlation plot in figure 4.2. In that same figure the distribution of the convergence shows a peak that indicates one main structure. A second peak would have been an indication for another structure comparable to the main structure, but this is not the case.

However, from the spatial distribution of the ellipticity in figure 4.3 it can be seen that there are a few odd orientations located near the z -axis. They have a high ellipticity, although their neighbouring points all have low ellipticity. Still, their convergence is high, just as for their neighbouring points. These points are also found in the upper right corner of the plot relating κ_{max} and e (figure 4.2). The origin of these phenomena is some little structure located at a reasonable distance from the centre of the main cluster. It is almost aligned with semi-principal axis a . When this structure is only just in the window of the inner region then the ellipticity will be very high, although the maximum convergence remains unchanged.

Just as for the CDM cluster, the same figures can be made for the WDM cluster. To start with, figure 4.4 shows the distributions of κ_{max} and e and their correlation. In comparison to the CDM case, now there is essentially no correlation. This is due to the amount of structure, which results in a range of ellipticities independent from the maximum convergence. When looking at the histogram of the convergence, then there are two peaks at around 1.8 and 2.4. This indicates two comparable structures, but with the latter one being the slightly more prominent, main structure. The amount of structure found in the WDM cluster, relative to the CDM cluster, is according to expectation as explained in section 1.1.

These two structures can also be derived from the spatial distribution of the convergence and the ellipticity in figure 4.5. The high convergence of the main structure is aligned with the z -axis. Also a second region of high convergence can be seen, which

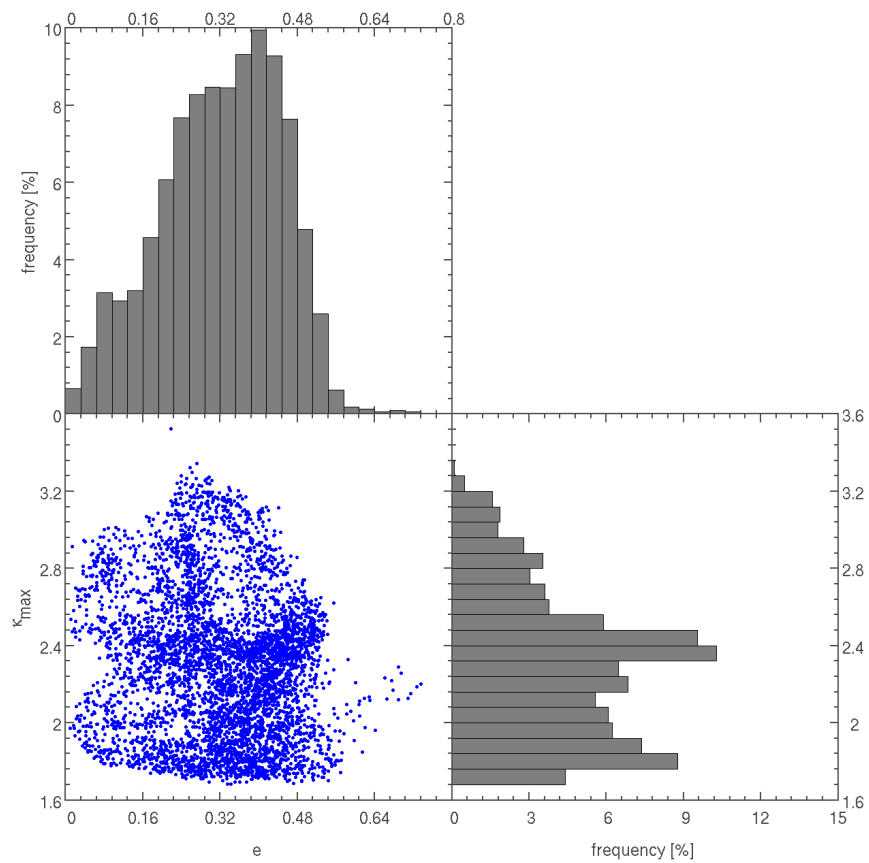


Figure 4.4: Distributions of the ellipticity (top left) and the maximum convergence (bottom right) and a plot of the convergence as a function of the ellipticity (bottom left). All results based on 5000 different rotations of the WDM cluster.

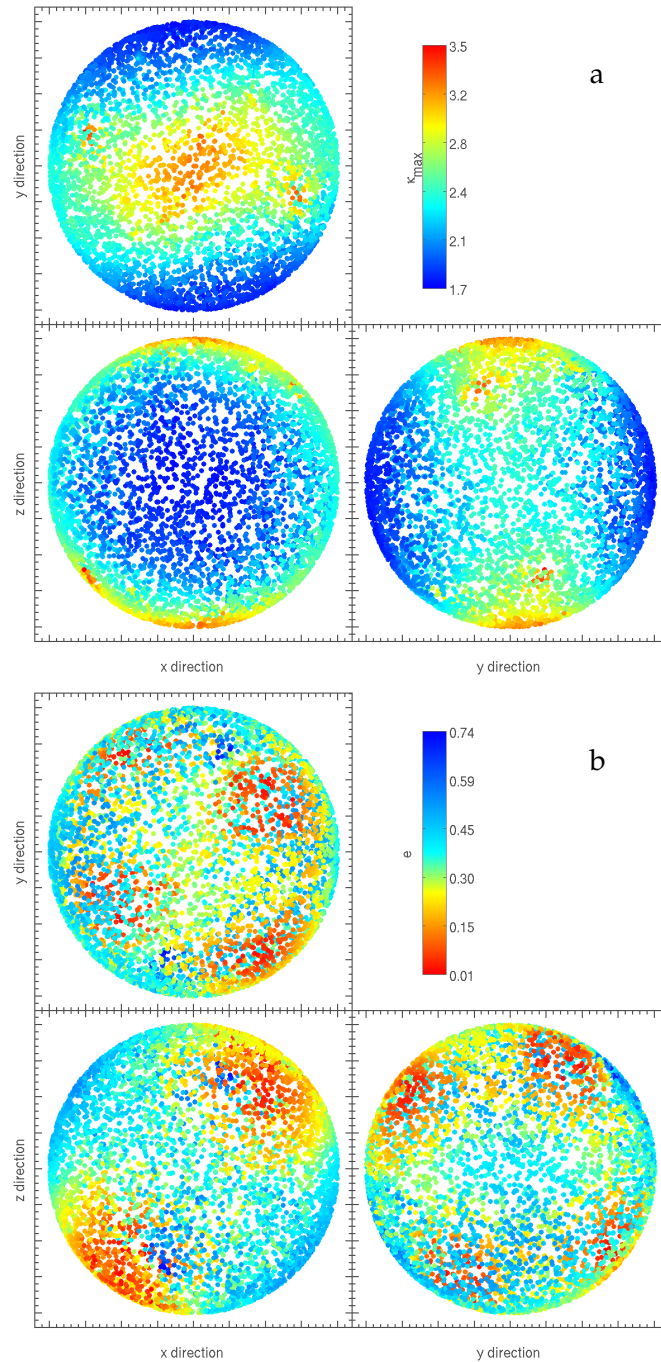


Figure 4.5: Projections of a) the maximum convergence (three top plots) and b) ellipticity (three bottom plots) as a function of the orientation of the WDM cluster. The line-of-sight of an orientation corresponds to the position of the point in that direction on a sphere with its origin in the centre of the plots. The strength of the quantities is represented by the colour of the points. Note the different colour scaling for the two quantities.

corresponds to the second structure. This smaller structure is located at a relatively small distance from the central part of the cluster. When looking at the spatial distribution of the ellipticity, then there are clearly two directions of low ellipticity. However these directions do not coincide with the directions corresponding to the high convergence regions. This should not come as a surprise when reminding that there was also no correlation between κ_{max} and e . No further explanation for the distribution of e is available.

Caustic areas — When discussing the areas enclosed by the caustics, it is good to remind that a high convergence results in a big radial caustic (section 2.2). In case of the tangential caustic, this caustic will become larger when the asymmetry of the lens increases.

Now first the area of the total, tangential and radial caustics are investigated in relation to the convergence as shown in figure 4.6. The first clear relation is $A_t \propto -\kappa_{max}$. The tangential caustic will increase when the ellipticity is higher, so that explains why a low convergence relates to a big tangential caustic. There is considerable amount of spread in the tangential caustic area, which is partly due (and similar) to the spread in the $e-\kappa_{max}$ correlation. This can be seen from the fact that A_t relates more nicely to the ellipticity, as can be seen from the colours of the data points in the plot. This is confirmed by the plot in the supplementary figure B.1. (The figure is analogous to figure 4.6, but the areas are related to ellipticity instead of convergence.) So essentially the main correlation should be written as $A_t \propto e$.

Another clear positive correlation is between A_r and κ_{max} . But it must be noted that when the convergence is below about 1.6, then the radial caustic area is zero or almost zero. Also the distribution of A_r shows that the radial caustic is smaller than 10 arcsec² for more than 65% of the orientations. This also results in the low average for this quantity in figure 4.1.

The correlation plots of the caustic areas show a clear dependence upon each other. The total area enclosed by all the caustics is roughly linearly dependent on both A_t and A_r , so the approximation $A_{tot} \approx A_t + A_r$ seems valid. A_{tot} is dominated by the tangential area if $\kappa_{max} < 2$ roughly, but mostly influenced by the A_r when $\kappa_{max} > 2$.

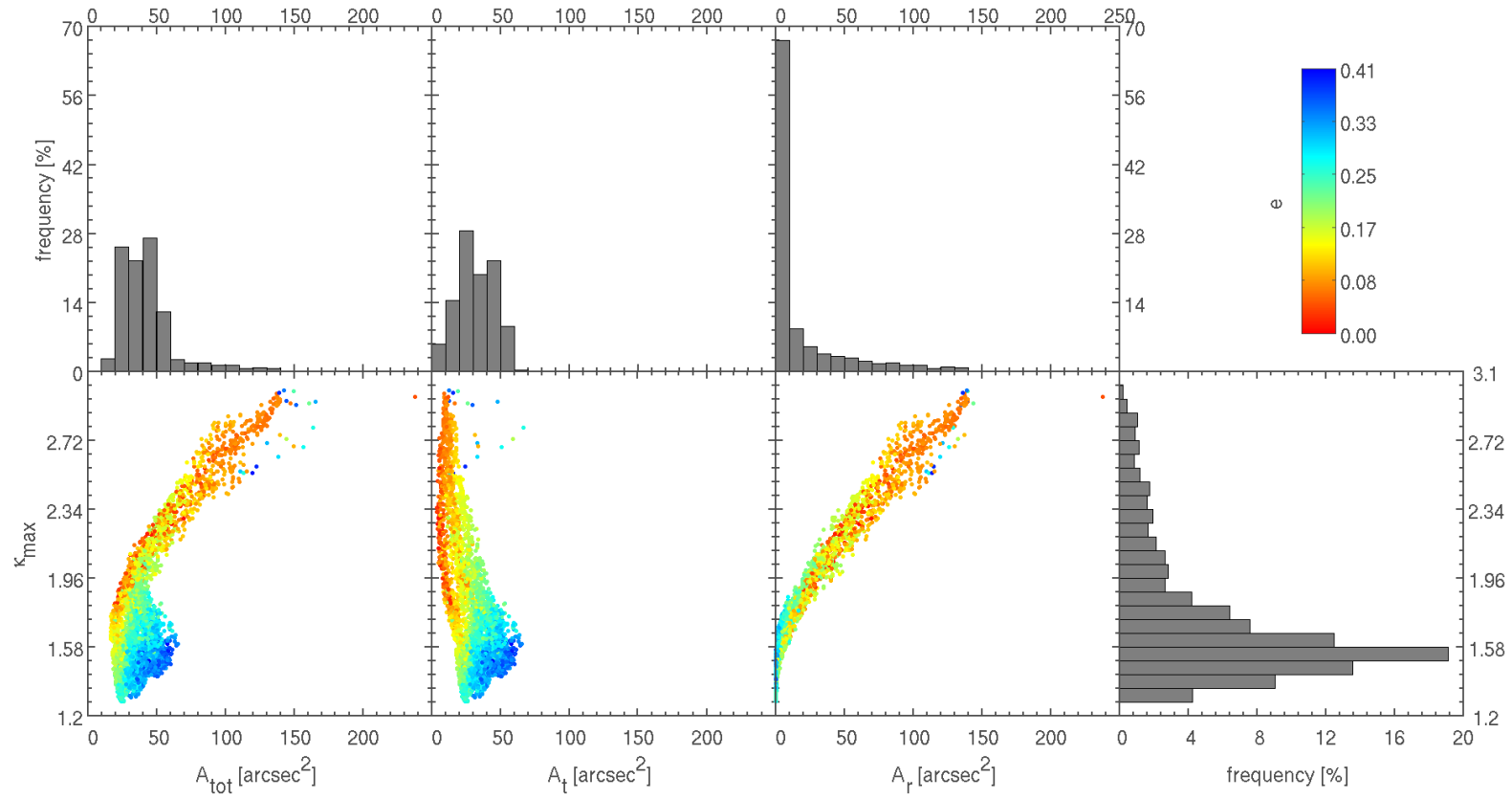


Figure 4.6: The distributions (top row) and correlation plots (bottom) of the total (first column), tangential (second column) and radial caustic area (third column) with the maximum convergence for the CDM cluster. The bottom most right plot shows the distribution of the maximum convergence. The colour coding of the points represents the ellipticity.

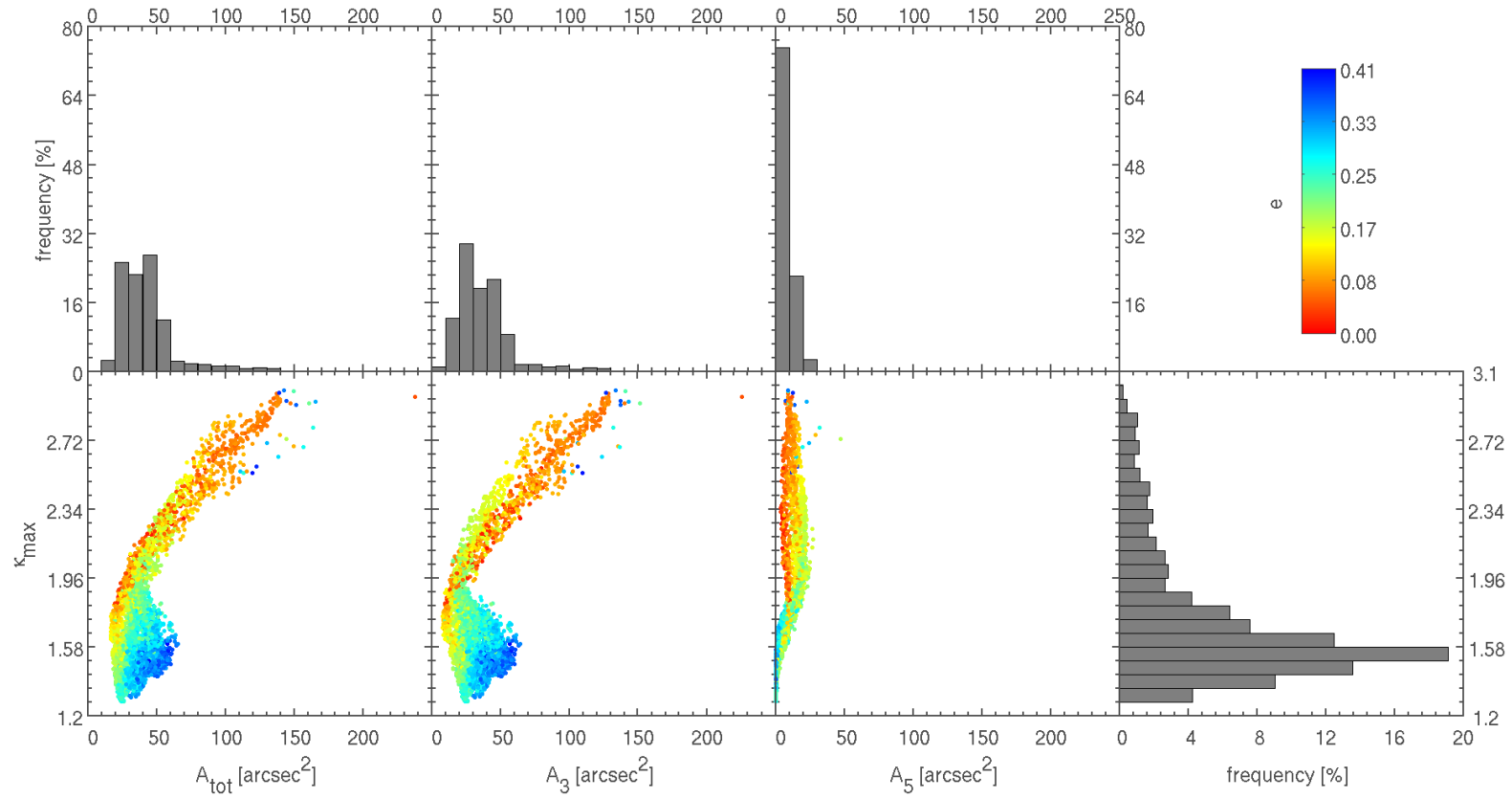


Figure 4.7: The distributions (top row) and correlation plots (bottom) of the total (first column), 3 images (second column) and 5 images caustic area (third column) with the maximum convergence for the CDM cluster. The bottom most right plot shows the distribution of the maximum convergence. The colour coding of the points represents the ellipticity.

The caustic areas corresponding to multiple images are given by $A_5 = A_t + A_r - A_{tot}$ and $A_3 = A_{tot} - A_5$. From the approximate relation $A_{tot} \approx A_t + A_r$ that seemed to hold in figure 4.6, it can be concluded that the quantity A_5 should roughly vanish and so $A_3 \approx A_{tot}$. This is confirmed when looking at the actual values for the A_5 and A_3 in figure 4.7. The total caustic area is indeed approximately equal to the caustic area resulting in three images. Also the distribution of A_5 shows that $A_5 < 30 \text{ arcsec}^2$ for almost all orientations.

The following step is to see what features are present in the results for the WDM cluster and which of these features are different from the CDM case. Therefore similar figures relating the convergence with the caustic areas are created. To begin with, figure 4.8 shows A_{tot} , A_t and A_r versus the maximum convergence. The relation $A_r \propto \kappa_{max}$ clearly emerges again, just as for the CDM cluster, although with a bit more spread. A difference is that there are no rotations any more for which the radial caustic vanishes. Actually only 5% of the rotations has $A_r < 10 \text{ arcsec}^2$, versus 65% in case of CDM. The WDM cluster differs from the CDM cluster in two ways, namely by its mass and its structure. The higher mass of the WDM cluster is most likely the cause of the higher values for the convergence. Subsequently that is also why the radial caustic is always present. More on this in the discussion in the last section.

The tangential caustic is related to the amount of asymmetry in the lens, due to structure and/or ellipticity. The WDM cluster does not show a nice correlation between A_t and κ_{max} . Still in general it can be said that the tangential caustic gets bigger for higher values for the convergence. This is really the opposite of the CDM cluster in which the result showed an anti-correlation. Even the correlations between the caustic areas and the ellipticity for the WDM case do not shine any light on this matter, as they do not show any trends (colour of the points in figure 4.8).

Furthermore, the total caustic area is a slightly neater/thinner version of the plot of the tangential caustic. This would mean that the approximate relation $A_{tot} \approx A_t + A_r$ seems to hold again (just as for the CDM case). Consequently the caustic area of five images should be small. A closer look at the plots with convergence versus the caustics areas of multiple images in figure 4.9 is needed to check this. It is true that the A_3 - κ_{max} plot has a similar shape as the total caustic area plot, but it is a little bit skewed. This is also confirmed by the correlation plot of A_5 , which reveals that A_5 is roughly linearly related to κ_{max} .

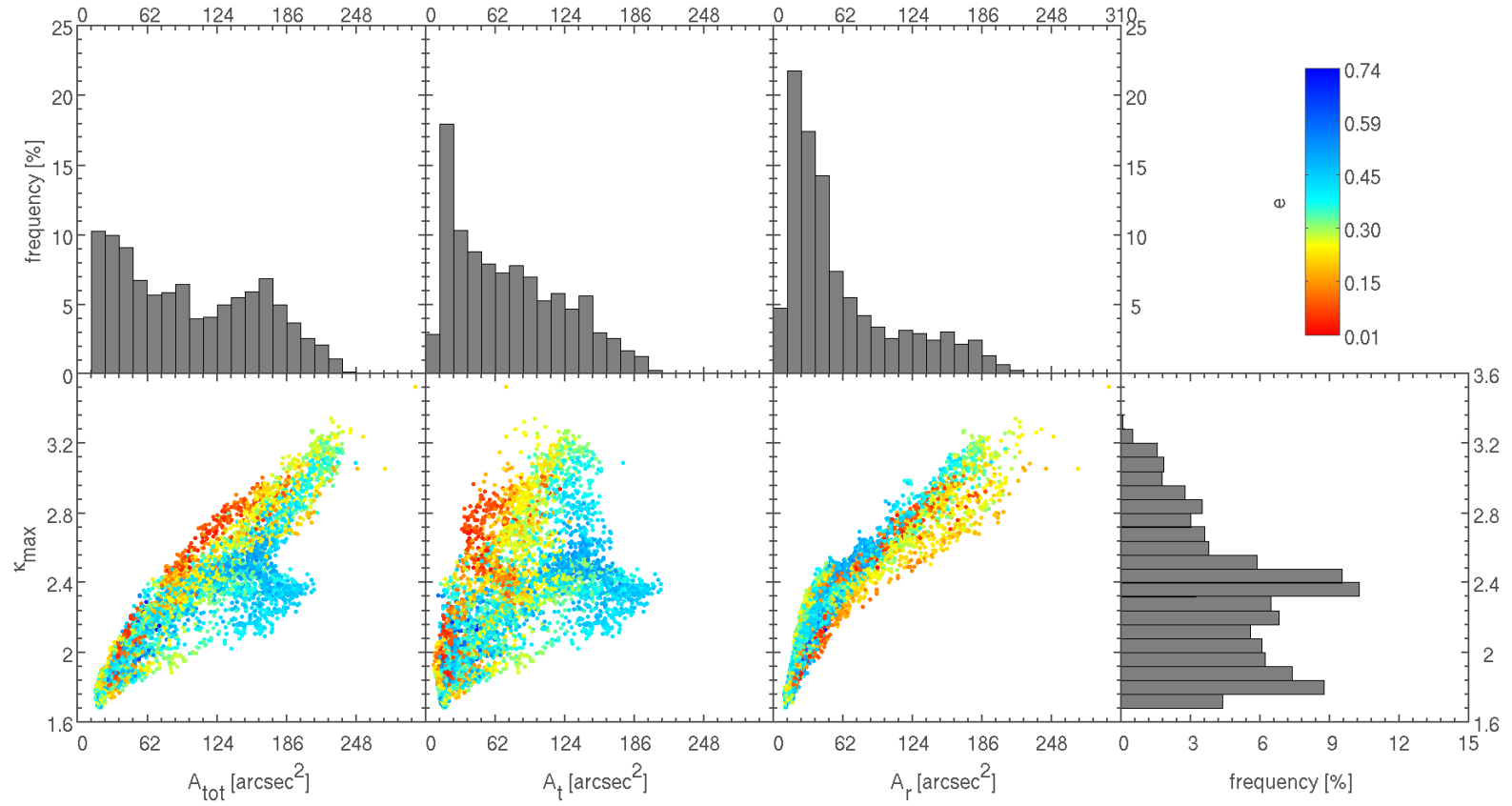


Figure 4.8: The distributions (top row) and correlation plots (bottom) of the total (first column), tangential (second column) and radial caustic area (third column) with the maximum convergence for the WDM cluster. The bottom most right plot shows the distribution of the maximum convergence. The colour coding of the points represents the ellipticity.

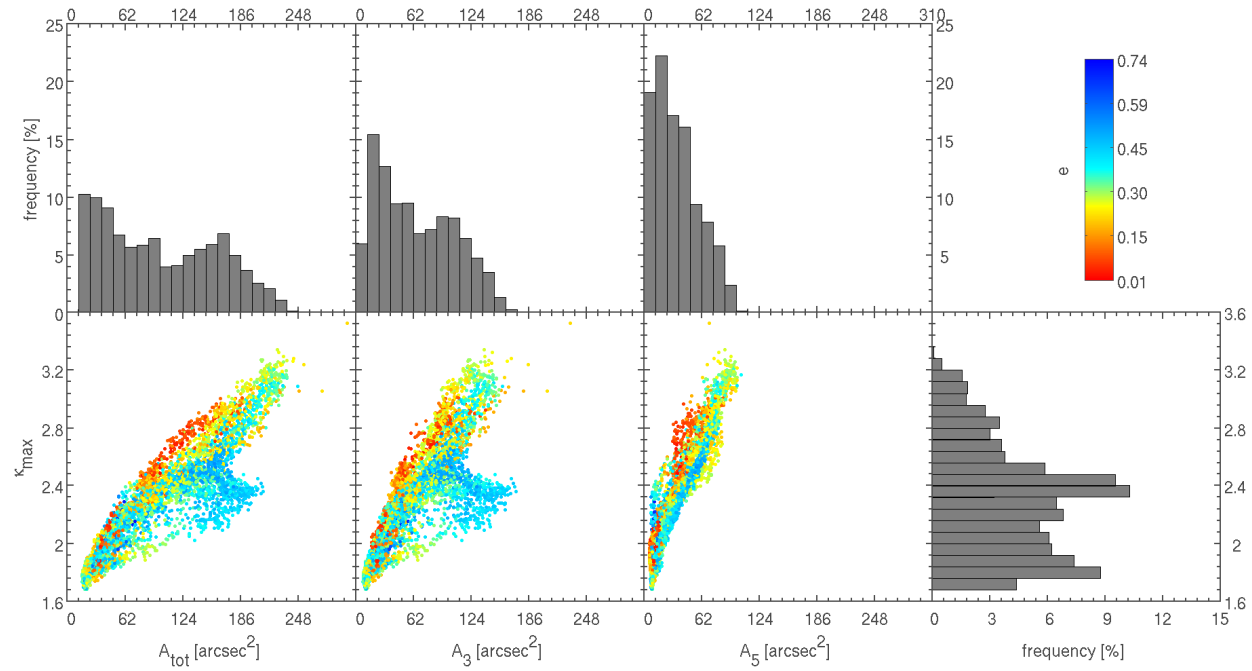


Figure 4.9: The distributions (top row) and correlation plots (bottom) of the total (first column), 3 images (second column) and 5 images caustic area (third column) with the maximum convergence for the WDM cluster. The bottom most right plot shows the distribution of the maximum convergence. The colour coding of the points represents the ellipticity.

Shear — The most interesting correlation would be finding one between one of the shear quantities and the maximum convergence and/or the ellipticity. First the quantities are recalled that are used to characterize the shear. The quantities γ and ϕ denote the total amplitude and the direction (corrected for the circular direction expectation) of the shear, respectively. Then the following quantities are calculated for each concentric annulus, which partitions the whole shear map,

- $\bar{\gamma}$: the average of the amplitude γ ,
- σ_γ : the standard deviation of the amplitude γ ,
- $\bar{\phi}$: the average of the angle ϕ , and
- σ_ϕ : the standard deviation of the angle ϕ .

Finally these quantities are averaged over all annuli and these final values are used in this section, still denoted by the same symbols. The result consists of eight values for each rotation of a cluster as this is done for both total and inner region.

To investigate a possible correlation with the maximum convergence, figure 4.10 shows the κ_{max} versus the shear parameters of the outer region for all rotations of both clusters. (The two top rows contain CDM calculations and two bottom rows present the WDM results.) There is a nice correlation between the convergence and $\bar{\gamma}$, where the slope of a linear fit is about 16 when all points are used. If the data is split when there seems to be a kink, then the slopes of the two separate curves are 11 and 23. It can be explained by the fact that a higher convergence results in bigger lensing effects. Note that more than half of the rotations of the CDM cluster have $\bar{\gamma} < 0.2$, corresponding to a $\kappa_{max} < 1.7$ (see figure 4.7).

For the CDM cluster, the remaining correlation plots of the shear quantities do not show such a nice dependence. They only contain a very rough anti-correlation with κ_{max} . Where more than 50% of the orientations have $\bar{\gamma} < 0.2$, they also have values $\bar{\phi} > 0.15$ and $\sigma_\phi > 0.11$. They all have a high ellipticity, indicated by the colours of the data points. But in general the ellipticity does not seem to correlate to the shear any better than the convergence, except for the property σ_γ . In figure B.2 in appendix B a similar plot as figure 4.10 is given, but with the convergence exchanged with the ellipticity. This figure shows a somewhat nicer correlation between e and σ_γ , while the other figures show even more spread. This relation $\sigma_\gamma \propto e$ suggests that the shape of the cluster directly influences the range of values for γ in the annuli around the centre.

All these relations become even more interesting when these results are compared to the case of the WDM cluster. Then the nice correlation for $\bar{\gamma}$ and the convergence emerges again. At first sight it seems that the slope of the linear fit is different as it is 9, approximately half the value for the CDM cluster. But when looking at the slopes of the data before and after the kink, then the slopes are 8 and 20, respectively. This corresponds

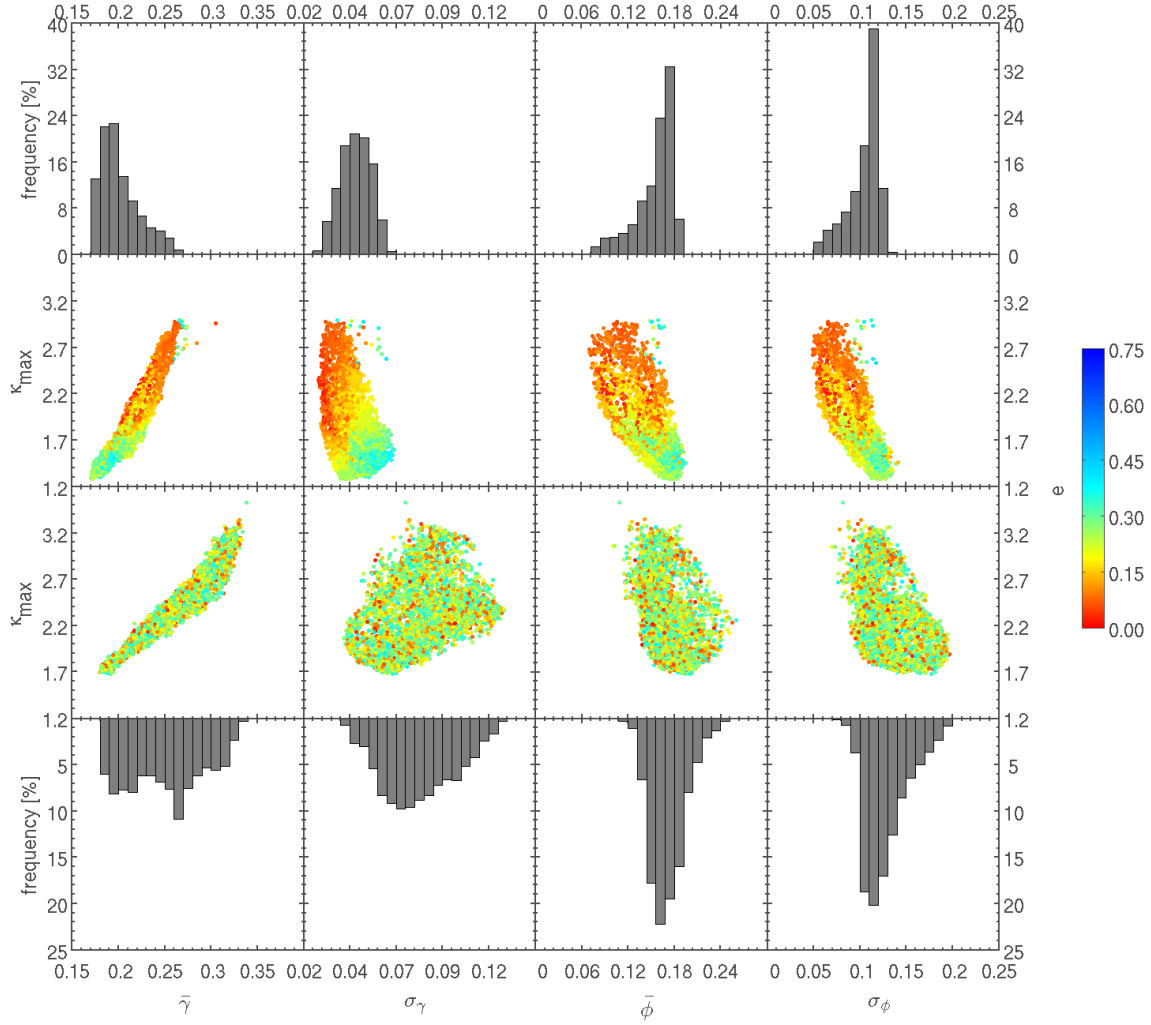


Figure 4.10: The distributions of the shear parameters (top row) and the correlations of these parameters with the maximum convergence (second row), where the shear of the outer region of the CDM cluster is used. Analogously the WDM cluster results are presented in the two bottom rows. The colour coding of the points represents the ellipticity.

well with the results for the CDM cluster (being 11 and 23). An actual difference is the ellipticity, which is now completely uncorrelated. More on this at the end of this section.

Surprisingly, when ignoring the huge amounts of spread, there is a positive trend in the $\sigma_{\gamma-\kappa_{max}}$ plot, which is the reverse of what is seen in the CDM cluster. Also the plots of the ϕ -quantities contain a lot of spread. Still the plots correspond reasonably well to the CDM case, but again the ellipticity seems randomly distributed. This will be discussed in the following paragraph. A nice feature of $\bar{\phi}$ and σ_{ϕ} in the CDM cluster was that their distribution had an increasing start and after the peak the distribution fell off very quickly. Conversely those distributions for the cluster with WDM show almost immediately a peak followed by a decreasing tail. These quantities $\bar{\phi}$ and σ_{ϕ} were expected to relate to the ellipticity, but no such thing is observed in the results.

Coming back to the ellipticity of the WDM cluster, a big difference with respect to the CDM cluster is that the ellipticity (represented by the colour of the data points) does not seem to correlate to the shear at all. As a confirmation one can have a look at the plots of the ellipticity versus the shear parameters in the supplementary figure B.2. It could all be expected already from the fact that also no correlation between the ellipticity and convergence was found. Still some shear quantity could have related to the ellipticity better than to the convergence, but evidently, this is also not the case.

Just as for the outer region, shear correlations were also investigated for the inner region. No significant differences were observed, so these results are not discussed any further. Similarly, the shear parameters were related to the caustic areas, but without yielding any new information. Therefore these correlations are not treated in this report.

4.2 Magnification probability distribution

In this section the probability distribution will be shown of the total magnification of a source with a given radius. This radius is important, as a bigger source will make the distribution be cut off at lower magnifications. Also the magnification is calculated by dividing the total area of the images by the area of the source. That is the reason why the source should not be taken too small, otherwise the calculation will have a too low resolution. This would give rise to a considerable amount of noise. For example, a source with the size of one pixel will result in a resolution in the magnification of one. The noise in the calculation will be discussed in the final section. The sources that are used cover an area of 100 pixels (on average). With the use of the pixel size (table 3.2), the radius of a source in the outer region is $13 \text{ arcsec} \approx 8 \theta_E$ and for the inner region this corresponds to $0.8 \text{ arcsec} = 0.5 \theta_E$. Further discussion on the source size will also be given in the final section. The number of sources that are used to characterize the outer region is always around 100.000 and similarly the inner region is probed using 200.000 sources.

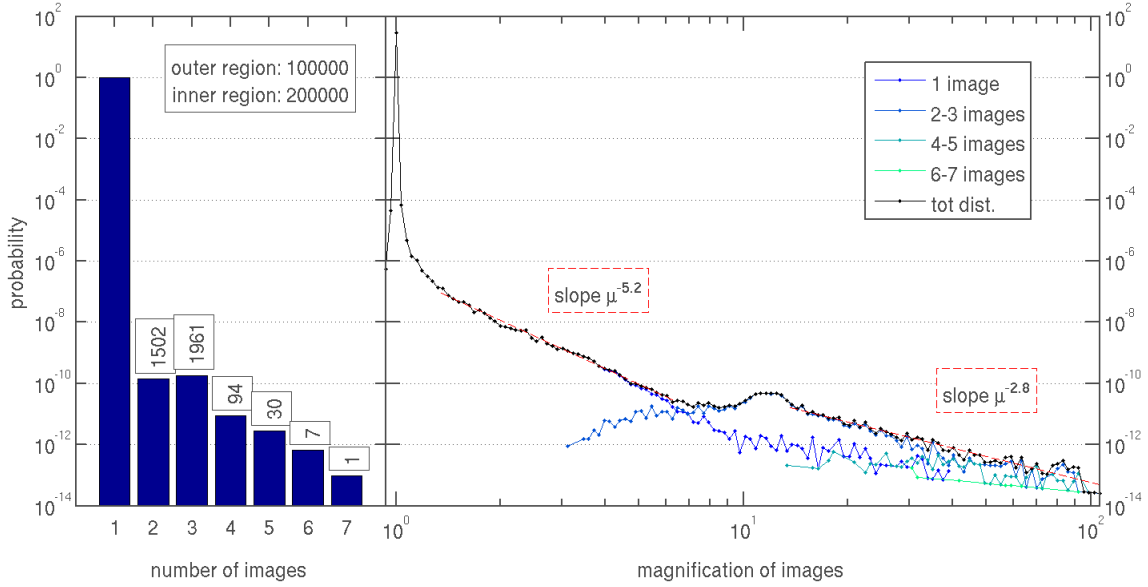


Figure 4.11: Probability of a source producing some number of images (left) and the source magnification probability distribution (right) for the rotation of the CDM cluster for which the maximum convergence, κ_{max} , is maximal. For more details, see text.

The first distribution that will be considered is given in figure 4.11. It shows the magnification probability distribution for the CDM cluster with the orientation for which the maximum convergence is maximal. There is a lot of information in these plots. On the left, the probability is shown, that a certain number of images arise from the given source. For each probability it is also shown upon how many sources the value is based. Also denoted in the upper half of the plot is the actual number of sources that is used to probe the outer and inner region. On the right the probability distribution is given of the total magnification of the sources. Besides the total distribution, also the distribution of the total magnification of 1 image, 2 and 3 images, 4 and 5 images and so on are given. A source always has one image, but every time the source crosses a caustic, one or two extra images emerge. This is one reason for presenting these sub-distributions. When a sub-distribution is calculated based on only a few sources (for example the 6-7 images distribution in figure 4.11), then the distribution will not be very accurate. The total distribution is also fitted with a power law for a manually selected range. In most cases an interval is chosen in which some sub-distribution is the main constituent of the total distribution and/or where the data points seem to follow an apparent linear trend. It is depicted by the red dashed line, including a denotation of the fitted power. Note that a relation purely described by one power law emerges like a straight line due to the double logarithmic axes with a slope equal to the exponent of the power law.

Some attention must be paid to the fact that the magnification probability can be

greater than one. This is due to the logarithmic scale of the x -axis. The logarithmic bin width is 0.015. This means that the actual bin width increases with increasing magnification. For example, the bin width is lower than one when $\mu < 70$ (roughly) and greater than one if $\mu > 70$. The distribution is calculated like a histogram, so the "probability" to get a magnification inside a larger bin would be higher. To correct for this the values of the histogram must be divided by the actual bin width. So the probability distribution can be seen as a sampled version of the function $P(\mu)$ given in formula 3.3. Around $\mu = 1$ the distribution will reproduce the delta-function. Since the delta-function cannot be resolved by means of a finite bin, the probability for that bin can become greater than one.

One prominent feature is the narrow peak around magnification 1. This is because of the fact that gravitational lensing only affect the small patch of sky around the galaxy cluster. The rest of the sources in the sky is not magnified and so their images have magnification one. Note that this was not actually calculated, but included manually when calculating the total distribution from the outer and inner region (as explained in section 3.3). Another feature is the probability of having magnifications lower than one. This is not a result, but the numerical uncertainty (noise) in the calculation of the magnification. This will be dealt with in the following discussion section.

In all of the following results, the sources that were placed in the outer region did not result in multiple images. From now on, the distributions corresponding to the CDM rotation where κ_{max} is maximal, will be denoted by $\text{CDM}|\kappa_{max}$.

Going back to the specific distributions of $\text{CDM}|\kappa_{max}$ in figure 4.11, the slope of the high- μ tail behaves like a power law with power $\mu^{-2.8}$. This corresponds almost to the -3 which came out of the theoretical consideration of a galaxy cluster in section 3.4. This result is also found when looking at the same plots for the case when the cluster's orientation corresponds to a maximum caustic area of 5 images, referred to as $\text{CDM}|A_5$ and given in figure 4.12.

In order to investigate the differences between the two cases, the convergence and caustics of both situations are also taken into consideration. The convergence map and the caustical curves can be found in the supplementary figures B.3 and B.4. The shapes of the two sets of caustics clearly show a big difference. For $\text{CDM}|\kappa_{max}$ and $\text{CDM}|A_5$, the area A_5 is 9.0 and 47.3 arcsec², respectively, as listed in table 4.1. The shape and area can explain a lot of features in the distributions.

An immediate effect of the different values of A_5 can be seen in the probability of getting 5 or more images. Whereas $\text{CDM}|A_5$ produced 5 images for 506 sources, $\text{CDM}|\kappa_{max}$ did only for 30 sources. The shape of the caustic is the cause for the maximum magnification produced, because a source is magnified considerably when it is laying on a caustic. A source laying on the caustic in case of $\text{CDM}|A_5$ will not be magnified as much

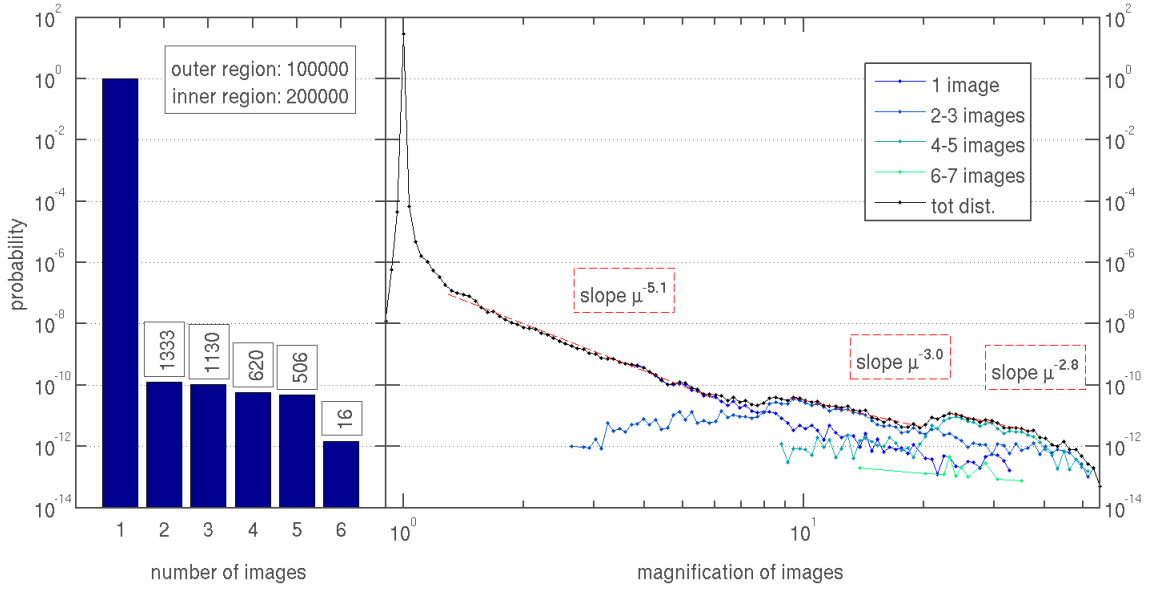


Figure 4.12: Probability of a source producing some number of images (left) and the source magnification probability distribution (right) for the rotation of the CDM cluster for which the caustic area of more than 5 images, A_5 , is maximal.

cluster	orientation	κ_{max}	e	A_t	A_r	A_{tot}	A_3	A_5
CDM	κ_{max}	2.99	0.35	12.7	139.2	142.8	133.9	9.0
	A_5	2.73	0.18	58.9	132.9	144.5	97.2	47.3
	e	1.50	0.41	44.8	0.6	44.8	44.2	0.6
WDM	κ_{max}	3.53	0.22	71.8	299.4	301.1	231.0	70.1
	A_5	3.17	0.37	128.8	206.6	230.6	125.8	104.8
	e	2.20	0.74	32.0	44.5	61.2	45.9	15.3

Table 4.1: Properties of the clusters for orientations when some quantity is maximal. The caustic areas A are given in units of arcsec^2 .

as a source on the caustic for $\text{CDM}|\kappa_{max}$. This is because the latter caustic is much more condensed. Coming back to the caustic area, the total number of sources that resulted in multiple images was about 3600 for both cases. This can be explained by the similar area enclosed by the total caustics, A_{tot} .

Interesting features are the bumps that occur in the tail of the magnification probability distributions. A bump corresponds to the situation where a source crossed the caustic and resulted in an extra pair of images. A first bump will correspond to a maximum in the distribution of 2-3 images. Here the order of the bump corresponds to the number of extra pairs formed. These bumps are visible in both $\text{CDM}|\kappa_{max}$ and $\text{CDM}|A_5$ at a magnification of about $\mu = 10$, although less prominent in the $\text{CDM}|A_5$ case. But, this latter distribution even has a second bump, which is due to an extra, second pair of images formed when the source crosses the second caustic.

Returning to the power law fitting, after the first bump the distributions are very similar and fit by a power law with almost the same exponent, -2.8 for $\text{CDM}|\kappa_{max}$ and -3.0 for $\text{CDM}|A_5$. In addition, the distribution of the $\text{CDM}|A_5$ configuration could also be fit for higher magnifications, after the second bump. The power of this fit is -2.8 , so it seems that here the expected dependence on μ still holds. Even a fit is made of the distribution at low magnifications where it is linear, so below a magnification of about 10. Also these values correspond to each other, where the slope of $\text{CDM}|\kappa_{max}$ is -5.2 and for $\text{CDM}|A_5$ it is -5.1 .

To see where the ellipticity comes in, also the CDM cluster orientation is considered for which the ellipticity is maximal, $\text{CDM}|e$. This distribution is given in figure 4.13. Because the ellipticity is high, the convergence is very low, the caustics are small and A_5 almost vanishes (see table 4.1). That is the reason why there are no sources that resulted in more than 3 images. Even the number of sources that had multiple images is only about 1100.

There are a couple of differences of $\text{CDM}|e$ with respect to the previous situations. One of them is that the distribution does not extend up to large magnifications. This feature is due to the large source size relative to the small caustic. This will be considered in the following discussion section. A consequence is that no high-magnification tail is present and so no fit is made of this region. The low- μ region could be fitted and is proportional to $\mu^{-4.9}$, which is similar to our previous results. Although lacking a high- μ tail, still there is a first bump at a magnification of about 20. This is different from $\text{CDM}|\kappa_{max}$ and $\text{CDM}|A_5$ as their first bump occurred around $\mu \approx 10$.

The next step is to look at the features that are present in the distributions of the WDM cluster. The same configurations for the WDM cluster will be considered as for the CDM cluster. To start with, figure 4.14 gives the distributions for the $\text{WDM}|\kappa_{max}$ situation. At first sight the results look similar to the ones of $\text{CDM}|A_5$, but there are some differences.

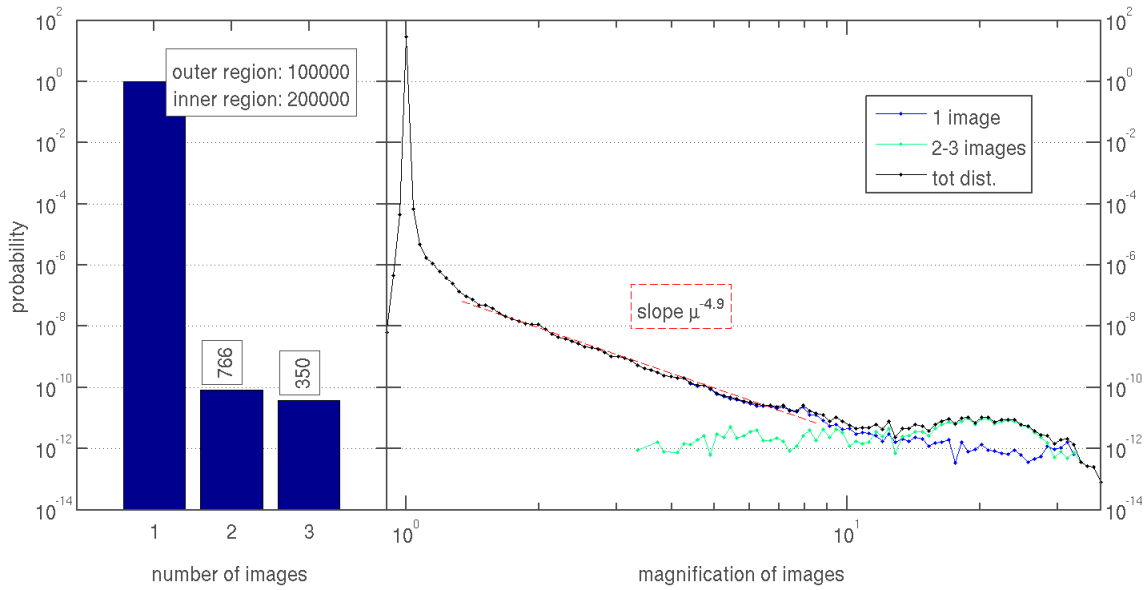


Figure 4.13: Probability of a source producing some number of images (left) and the source magnification probability distribution (right) for the rotation of the CDM cluster for which the ellipticity, e , is maximal.

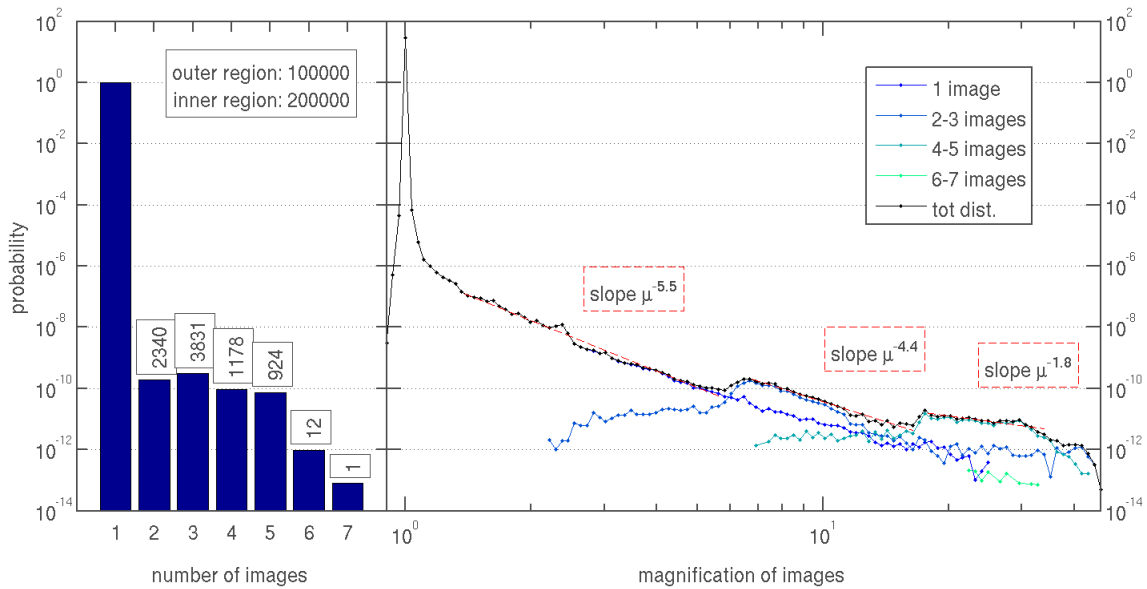


Figure 4.14: Probability of a source producing some number of images (left) and the source magnification probability distribution (right) for the rotation of the WDM cluster for which the maximum convergence, K_{max} , is maximal.

Firstly, all the caustic areas are bigger and so the total number of multiple imaged sources is about 8300 (versus 3600 for CDM| A_5). Also more sources resulted in 5 images in case of WDM| κ_{max} when compared to the CDM| A_5 situation, 924 versus 506. Subsequently the magnification probability distribution is less noisy at high magnifications and so features will become clearer. Another difference is shown when looking at the power-law fits. The figure shows that the slopes are -4.4 after the first bump and -1.8 after the second. This means that the μ^{-3} dependence of the tail is not observed any more. The two fits are not even the same, but more on this will be said when more results are available. For the rest it can be said that the fitted slope of the low- μ region is only slightly lower than the ones found for the CDM cluster. Another similarity with the CDM cluster is that the bumps are again nicely present in the WDM case, without any important differences.

Another set of distributions is shown in figure 4.15, where the WDM cluster is rotated with A_5 maximal. This figure is rather similar to the previous case, WDM| κ_{max} . But the total caustics are smaller and so this results in a bit fewer sources with multiple images, as there are about 7900 of them. On the other hand there are more than twice as many sources with 5 images when comparing WDM| A_5 to WDM| κ_{max} , because the property A_5 is larger. Because of this, the first bump is almost invisible, while the second is still clearly distinguishable. So the first/second bump becomes less visible when the area A_3/A_5 gets smaller relative to the total caustic area. Remarkable are the two fits of the high- μ tail of WDM| A_5 after the first and second bump, being -3.2 and -3.4 respectively. These slopes are just a bit steeper than the expected proportionality μ^{-3} . In the WDM| κ_{max} configuration the slopes had completely different values. This matter will be discussed further in the following section. Now, the low-magnification slope (before the first bump) is flatter than all other cases considered so far (both CDM and WDM) as it is -4.6 .

Finally the distribution of the maximum ellipticity configuration is considered as given in figure 4.16. Although the caustic areas for this case are small for a general rotation of the WDM cluster (compare values in table 4.1 with figure 4.1), still there is a reasonable amount of sources with multiple images. No second bump can be observed because the caustic area A_5 is too small. Still the first bump features nicely in the distribution.

Not mentioned so far, but the maximum magnification in all three configurations of the WDM cluster seem to have strange values in comparison to the CDM outcomes. This can all be related to the shape of the caustics again. This will be explained in the following section, but no specific details will be given any more in this report. Also the distributions of other configurations were investigated, but the selection above summarizes the most important features and differences that occurred.

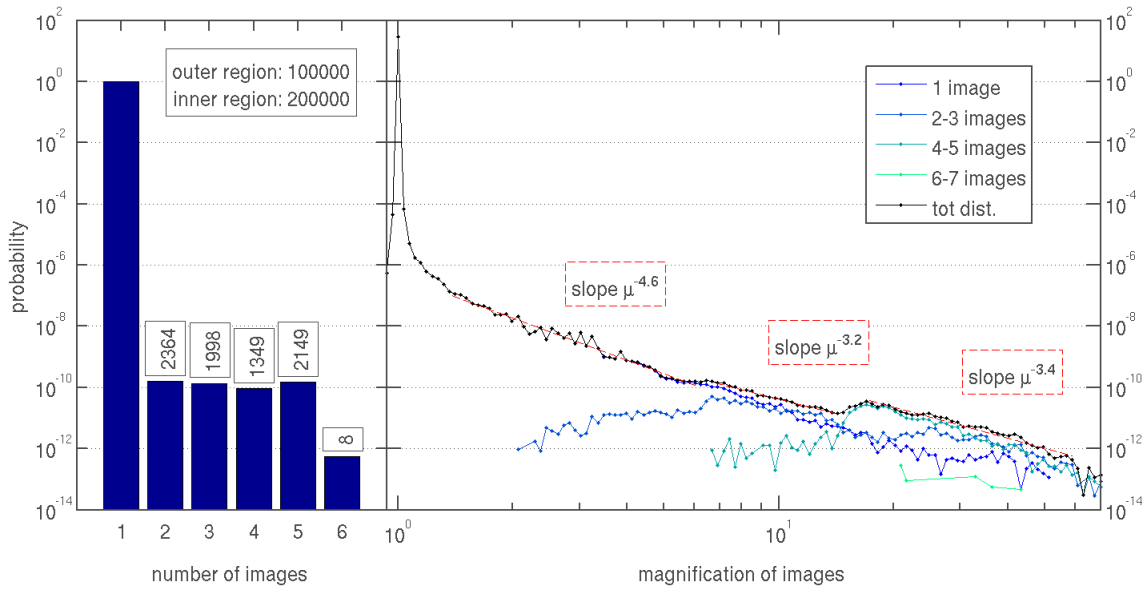


Figure 4.15: Probability of a source producing some number of images (left) and the source magnification probability distribution (right) for the rotation of the WDM cluster for which the caustic area of more than 5 images, A_5 , is maximal.

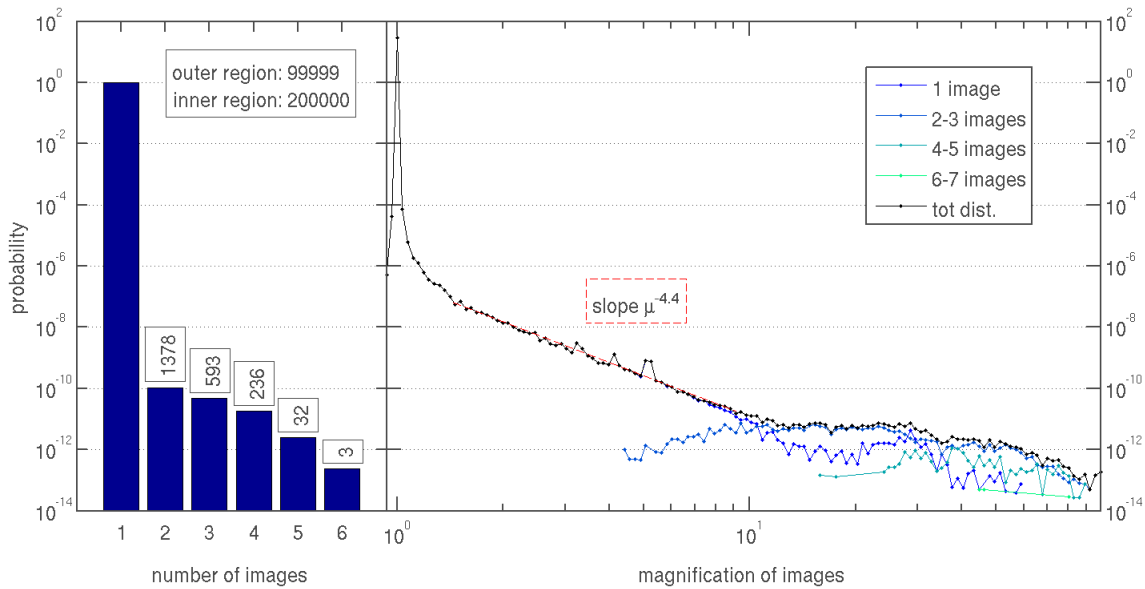


Figure 4.16: Probability of a source producing some number of images (left) and the source magnification probability distribution (right) for the rotation of the WDM cluster for which the ellipticity, e , is maximal.

4.3 Discussion

In this final section a few details will be discussed about the way the results were obtained, but also some details are given about the results themselves. The results showed a few similarities, but also differences between the CDM and WDM galaxy cluster.

General properties of calculated quantities — The box plot given in the beginning of this chapter (figure 4.1), shows a general feature for all calculated quantities (κ_{max} , e , caustic areas and shear characteristics). All quantities for the WDM cluster were approximately equal or greater than the ones of the CDM cluster. One part of the explanation could be that the WDM cluster contains about 25% more mass than the CDM one. More mass will result in a higher convergence, so in principle the caustic areas and shear of the WDM cluster distribution shift to higher values, with respect to the ones for the CDM cluster. The bigger radial caustic area is only partly due to a higher convergence, because another reason could be the amount of structure in a WDM cluster. More structure means more randomness in the shape of the cluster. That is why quantities like ellipticity and tangential caustic area can have more spread in their distribution (larger boxes in the figure). More structure also leads to higher shear properties.

Ellipticity — The determination of the ellipticity is somewhat troublesome. There are many ways to calculate it, but two methods were compared. The first method fits ellipses to the contours of equal convergence. Another method makes use of the second moments of the distribution (explained in appendix A.2). The problem emerged that the methods yielded rather different results. Eventually the choice was made to use the latter one, the second moment method. This choice was made, because it appears to be the most solid one as it depends on the least number of parameters. Moreover, the method is also used in other literature for calculating the ellipticity from a given distribution (see [13] as example).

The results showed a clear correlation between the convergence and the ellipticity for the CDM cluster. This can indicate that the cluster is very neat and without a lot of structure. Also the spatial distribution of κ_{max} and e showed nice patterns. Conversely, for the WDM cluster no such correlation between κ_{max} and e was found suggesting that it could not be described by a well-defined distribution of matter. The statistical distribution of κ_{max} even showed evidence for a second large structure, besides the main part of the cluster. So the WDM cluster seems to have more large-scale structure.

The statements about the structure of the clusters can be verified by looking at the actual three-dimensional distribution of the clusters. This is done after almost all of the results and discussion were written in order to perform an unprejudiced analysis. The spatial distribution nicely shows the structure that is discussed earlier, which confirms the outcome of the analysis.

Caustic areas — The CDM cluster results in a nice linear relation between the tangential caustic area A_t and the ellipticity e . This can also be seen as evidence for a neat structure describing the CDM cluster. This is a nice example conform the theory explained in section 2.2 of a distribution shaped like an ellipsoid. Again the WDM cluster does not show such a nice correlation. Ignoring the considerable amount of spread, one can roughly say that A_t depends linearly on the convergence, but it does not relate to the ellipticity at all. This can be seen as evidence that the WDM cluster is not described by a nice distribution. Another explanation is not available.

The relation $A_r-\kappa_{max}$ was similar for both the CDM and WDM cluster. Their results can even be combined in one plot, which shows that they exhibit the same relation. In gravitational lensing it is normal that a higher convergence results in a bigger radial caustic (see section 2.2). So this feature is independent of the lens.

Shear — In general, the shear is a property that is measured using observations, which is then used to determine the properties of a cluster. In this report the shear was calculated for a given cluster, followed by a characterization of it. There is no general way of doing this characterization. The results presented use one particular method, but there are many possibilities. The reason for calculating the shear properties for different annuli before averaging, is that it may incorporate the dependence upon the distance from the centre.

In the results it appeared that the shear parameters are the same for both inner and outer region. Not only the shape of the distributions are the same, but even one cluster orientation yields the same values for both regions. This is remarkable because the shear map of the inner region contains much more information about the structure, when compared to the shear map of the outer region. That is why one would expect much more detailed information to be contained in the inner region. A reason for its absence could be that the used method is not detailed enough to contain the extra information of the inner region. Perhaps a different characterization of the shear map would contain this information. This other method could be chosen so as to include a dependence upon the ellipticity, as the ϕ parameters failed to do.

The chosen characterization resulted in the parameters $\bar{\gamma}$ and σ_γ which related to κ_{max} and e , respectively. In case of the $\bar{\gamma}-\kappa_{max}$ relation, both clusters gave a nice positive relation, even the slopes of their partial fits matched, being around 10 and 20 for the data before and after the kink. The general feature can be explained by the fact that a higher convergence gives rise to bigger lensing effects and so also a greater shear. The reason for the two slopes is not yet clear.

For the relation $\sigma_\gamma-\kappa_{max}$, it is remarkable that the CDM cluster had a negative trend, whereas the WDM cluster had a positive one. But when looking at the $\sigma_\gamma-e$ correlation, then it becomes clear that both clusters show a positive relation. This can be explained

by the circular annuli for which σ_γ is calculated. An elliptical distribution has a larger range of values for the shear in such an annulus. Still the WDM results showed a lot more spread in their plots, which can be accounted for by the fact that the WDM cluster seems to have more structure.

Magnification, its probability distribution and source size — One feature of the probability distribution of the magnification is the power law exponent of the high- μ tail. With the use of [14] the power law exponent -3 can be checked. This article states that if the three-dimensional density profile behave like $\rho(r) \propto r^n$ then the high magnification tail should be given by $P(\mu) \propto \mu^{\frac{1-n}{1+n}}$. When this is calculated for the CDM and WDM clusters, then $n = -1.9$ for both clusters. Consequently also the magnification dependence of the tail should be $\mu^{-3.1}$ for both. This corresponds well to the presented results of the CDM cluster. But for the WDM cluster, this dependence is only correct for the case of WDM| A_5 , not the WDM| κ_{max} configuration. (For WDM| e it was not reasonable to make a fit.)

In order to check the exponent of the high- μ tail for the WDM cluster, extra calculations are done. In these calculations, magnification probability distributions are made for 25 random orientations of the cluster. Then the tails of these distributions are fitted, only when there was a clear linear curve due to a sub-distribution of one extra pair of images. Eventually 13 orientations were suitable, which had a power-law exponent ranging between -2.5 and -4.7 with an average of -3.9 . This is clearly not the power law expected from the theoretical treatment. The same calculation is done for the CDM cluster where 13 out of 35 distributions could be used. The exponent ranged between 2.4 and 4.3 with an average of 3.3, which is still reasonably as expected. The reason of the WDM cluster behaviour is not clear, but there are two aspects that should be kept in mind about the calculation of the distributions.

The first aspect is the uncertainty in the determination of the magnification. As mentioned earlier, this can account for magnifications lower than one that occurred in the results. The uncertainty is a result of the source being represented by an image, consisting of pixels. As the source position is not necessarily an integer value, the source will not always contain the same number of pixels. Consequently, when the images and their magnification are calculated, then this magnification will have a small uncertainty, because of the varying source size.

A source is parametrized by its (theoretical) area A_s , but actually its radius $\sqrt{A_s/\pi}$ is used to select the pixels that represent the source. The (absolute) difference between A_s and the actual number of pixels of which the source consists, will be the error denoted by ΔA_s . Figure 4.17 shows the maximum error versus the setting of A_s , in case of $N_\Delta = A_s \cdot 10^3$ random positions of that source. The figure also shows that the (maximum) error remains roughly below the estimate $\sqrt{A_s}$, assuming the source area is distributed like a Poisson distribution. The choice of $A_s = 100$ in calculating the results means that the error is $\Delta A_s = 4$.

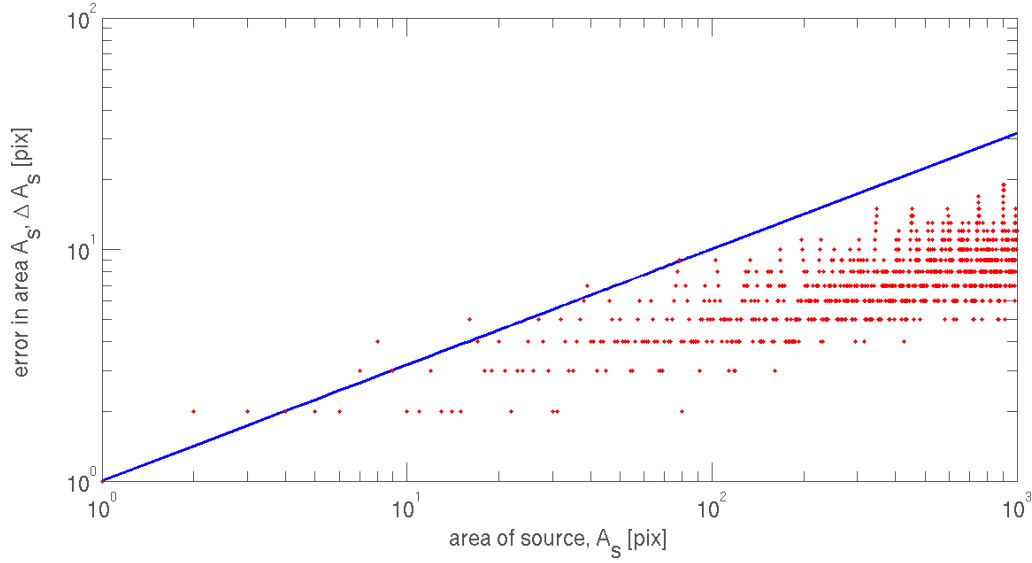


Figure 4.17: The area of a circular source A_s for which the maximum error in the area ΔA_s is calculated. This error is due to the representation of the source as pixels. See text for more details.

Besides the uncertainty in the source size, also the size itself can have important consequences, as the results already showed. A source that is big relative to the caustics, will not have a very high magnification. Conversely, small sources near a caustic will result in highly magnified images. This effect is further investigated by choosing different source sizes, namely 30, 80, 120 and 360 pixels and determine the magnification probability distributions in the $\text{CDM}|A_5$ situation. The distributions for $A_s = 30$ and 360 arcsec^2 are given in appendix B.2, in the figures B.5 and B.6. (The distribution in the $\text{CDM}|A_5$ case with a source of 100 pixels is given in figure 4.12.)

From these distributions the maximum magnification (μ_{max}) is taken and listed in table 4.2, along with some other characteristics. The theoretical source area A_s corresponds to a source of radius d_s . For N_Δ sources the position is taken randomly, after which the (absolute) difference between the actual and the set area is calculated. The maximum of this error in the area is denoted by ΔA_s . The table shows a clear negative relation between the maximum magnification and the source area. As the source gets bigger, μ_{max} will become smaller. In the $\text{CDM}|A_5$ case, the sources diameter $d_s = 3.00 \text{ arcsec}$ is roughly half of the size of the A_5 region of the caustic (caustics are shown in figure B.4). Because it is relatively big, only low magnifications will occur. Note also that the probability distribution is not properly sampled in case of the largest source, as the high-magnification tail of the distribution does not have the power-law exponent around -3 (figure B.6).

A_s [pix]	A_s [arcsec ²]	d_s [arcsec]	ΔA_s [pix]	N_Δ	μ_{max}
30	0.59	0.87	2	30000	80
80	1.57	1.41	2	80000	57
100	1.96	1.58	4	100000	55
120	2.35	1.73	4	120000	51
360	7.06	3.00	8	360000	38

Table 4.2: The circular source area (A_s) with the corresponding theoretical diameter (d_s) and the maximum error in the area (ΔA_s), due to the representation of the source by pixels. This error is based upon N_Δ calculations as explained in the text. Also the maximum magnification (μ_{max}) of the source magnification probability distribution is given for the orientation of the CDM cluster where the area A_s is maximal.

Influence of smoothing — The smoothing of the distribution from the GADGET simulation is needed to get a realistic mass distribution for a galaxy cluster. However, there is no prescription of what the exact amount of smoothing should be. As stated in section 3.2, the smoothing radius is chosen such that the maximum convergence for the inner and total region differ least and they do not start to drop. Besides this argumentation, no further investigation is done on the influence of the amount of smoothing.

Influence of distances/red shifts — After the galaxy cluster itself, the next most important input to the calculation are the red shifts of the lens and the source, z_l and z_s respectively. There is no specific reason for taking $z_l = 0.2$ and $z_s = 2.0$ other than being moderate values for those parameters in situations where gravitational lensing occurs.

In order to get a notion of the influence of these values, a selection of figure 10 from [15] is taken and shown in this report as figure 4.18. This figure nicely depicts the dependence of the caustics upon the red shift of the source plane (fixing z_l). The figure represents the three-dimensional shape of the caustic in which the distance from the observer (O) to the source is varied, given an elliptical lens (L). Note that the three middle rays represent horizontal rays in a plane perpendicular to the paper, Similarly the top, middle and bottom rays represent the vertical plane, parallel to the paper. Point A corresponds to the point where the horizontal rays of light come together in the source plane. When the source is located further away from the lens, then the light rays cross and point A becomes a curve with some finite extent. Note that this is the tangential caustic. Similarly the vertical light rays will cross each other from point B on, creating a three-dimensional object that will be the radial caustic when taking a slice at a certain red shift. A final remark about the figure is that the right end is not the end of the occurrence of caustics. For increasing distance of the source (from the observer) the tangential caustic will become smaller until it vanishes at some point. At a sufficiently large distance, even the radial caustic vanish again, after which the source will not be strongly lensed any more.

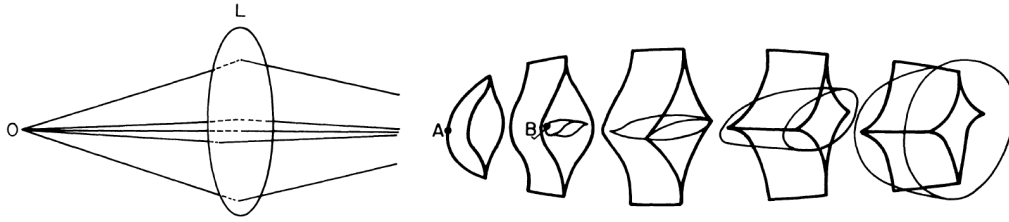


Figure 4.18: A representation of the three-dimensional shape of the caustics in which the distance from the observer (O) to the source is varied, given an elliptical lens (L). Note that the three middle rays represent horizontal rays in a plane perpendicular to the paper. Similarly the top, middle and bottom rays represent the vertical plane, parallel to the paper. Point A corresponds to the point where the horizontal rays of light come together in the source plane. Similarly, the vertical light rays cross at a point B. For more details, see the text. This figure is a selection of figure 10 from [15].

When looking at the caustics that occurred in the calculations, it can be concluded that they cover a large range of possible caustics, from the far left with only a tangential caustic, to the far right with a radial caustic and a very small tangential caustic. From this it can be said that the chosen red shifts are appropriate as almost all possible configurations are probed.

One versus many clusters — One final, but important point of discussion is the fact that one cluster for each cosmology is used to determine the properties of that cosmology. Of course, this is way too few to base any definite conclusions on, for a certain cosmology. What helps are the different rotations of one cluster, as this can result in a rather different appearance of the cluster. But as it is still the same cluster, for example, the strong correlation between convergence and ellipticity, valid for the CDM cluster, does not need to hold for other CDM clusters.

Moreover, one (or both) of the clusters used for this report could be a peculiar one by coincidence. In that case, a cluster would not represent a common cluster in that cosmology. The amount of structure in both clusters is as expected and so there is no indication that the clusters are a peculiar pair. Due to time limitations of this research project, no more clusters could be investigated.

5 Conclusions

A cluster in a universe described by the standard model for cosmology with cold dark matter (CDM) will have less large-scale structure compared to a cluster from a warm dark matter (WDM) cosmology. This report describes the pilot study to investigate the possibility of distinguishing between these two types of galaxy clusters, based on their gravitational lensing effects.

The investigation looked at the distributions and correlations for a range of quantities. The convergence and the ellipticity showed nice evidence for more large-scale structure in the WDM cluster compared to the CDM one. Also the analysis of other quantities confirmed this conclusion, or other relations were found that could be accredited as general features of gravitational lensing.

There were a couple of promising ways of analysis which may have the ability to identify the type of cosmology. In this report the shear was characterized by a few parameters. These parameters showed some nice relations for both cosmologies. The quantity related to the average amplitude of the shear ($\bar{\gamma}$) showed a positive correlation with the convergence. The spread in the shear amplitude (σ_{γ}) related rather nicely to the ellipticity. More investigation is needed to determine the potential of this method as other characterizations could result in parameters that relate even better with other quantities.

There was also one remarkable result that could be taken into account in further research. The probability distributions of the source magnifications behave at high magnifications conform the expected power law with an exponent of -3 , when the CDM cluster was considered. But looking at the WDM cluster, then this exponent was around -4 . A more detailed study could verify the reliability of this result, but if this result is correct, then this would have implications on the bias in observing the size of galaxies.

Although the clusters were as expected, the WDM cluster is 25% more massive than the CDM cluster. This difference in mass influenced the results, although this could easily be incorporated in the analysis of the two clusters. Still the galaxy clusters could be peculiar ones, not being representative for their cosmology. Therefore multiple clusters

should be used in future work continuing this research, giving a more reliable, overall picture for each cosmology. Also the dependence of the results upon the red shifts of the lens and the source should be included. This should be done in order to get a complete picture of the possibilities of identifying cosmologies based on the gravitational lensing effect of their galaxy clusters.

References

- [1] M. Persic, P. Salucci and F. Stel, *The universal rotation curve of spiral galaxies – I. The dark matter connection*, Monthly Notices of the Royal Astronomical Society, vol. 281.1, 1996, pages 27-47.
- [2] Y. Sofue and V. Rubin, *Rotation curves of spiral galaxies*, arXiv preprint: astro-ph/0010594, 2000.
- [3] Planck Collaboration, *Planck 2013 results. I. Overview of products and scientific results* arXiv preprint: 1303.5062, 2013.
- [4] P. Schneider, J. Ehlers and E. Falco, *Gravitational lenses*, Springer-Verlag Berlin, 1992.
- [5] R. Kormann, P. Schneider and M. Bartelmann, *Isothermal elliptical gravitational lens models*, Astronomy and Astrophysics, vol. 318, 1994, pages 285-299.
- [6] R. Kayser, P. Helbig and T. Schramm, *A general and practical method for calculating cosmological distances*, arXiv preprint: astro-ph/9603028, 1996.
- [7] R. Hockney and J. Eastwood, *Computer simulation using particles*, Taylor & Francis Group, 1988, pages 211-214.
- [8] M. Killedar et al., *How baryonic processes affect strong lensing properties of simulated galaxy clusters*, Monthly Notices of the Royal Astronomical Society, vol. 427.1, 2012, pages 533-549.
- [9] M. Bartelmann, *Numerical methods in gravitational lensing*, arXiv preprint: astro-ph/0304162, 2003.
- [10] P. Schneider, *An analytically soluble problem in fully nonlinear statistical gravitational lensing*, The Astrophysical Journal, vol. 319, 1987, pages 9-13.
- [11] Y. Hezaveh and G. Holder, *Effects of strong gravitational lensing on millimeter-wave galaxy number counts*, The Astrophysical Journal, vol. 734.1, 2011, pages 52-59.
- [12] K. Rauch et al., *Caustic-induced features in microlensing magnification probability distributions*, The Astrophysical Journal, vol. 386, 1992, pages 30-35.

- [13] A. Evans and S. Bridle, *A detection of dark matter halo ellipticity using galaxy cluster lensing in the SDSS*, *The Astrophysical Journal*, vol. 695, 2009, pages 1446-1456.
- [14] P. Valageas, *Weak gravitational lensing effects on the determination of Ω_0 and Λ from SNeIa*, *Astronomy and Astrophysics*, vol. 354, 2000, pages 767-786.
- [15] R. Blandford and R. Narayan, *Fermat's principle, caustics, and the classification of gravitational lens images*, *The Astrophysical Journal*, vol. 310, 1986, pages 568-582.
- [16] D. Kirk, *Graphics gems III*, Academic Press Professional, Inc., 1992, pages 117-120.
- [17] S. Bridle et al., *Handbook for the GREAT08 Challenge: An image analysis competition for cosmological lensing*, *The Annals of Applied Statistics*, 2009, pages 6-37.
- [18] F. Chang, C. Chen, and C. Lu, *A linear-time component-labelling algorithm using contour tracing technique*, *Computer Vision and Image Understanding*, vol. 93.2, 2004, pages 206-220.

Methods used

A.1 Random rotation matrix

The following algorithm can be used to perform a uniformly distributed random rotation on the unit sphere, which is also described in [16]. To do this rotation, the combination of the following two steps can be taken. First a random rotation around the north pole $z = (0, 0, 1)$ is done, followed by a second rotation which aligns the z -axis with a random direction.

The starting point of a random rotation are the three random numbers x_1, x_2 and x_3 , lying in the interval $0 < x \leq 1$. Firstly, a random rotation around the z -axis can be generated using x_1 , which takes the form of

$$R = \begin{pmatrix} \cos(2\pi x_1) & \sin(2\pi x_1) & 0 \\ -\sin(2\pi x_1) & \cos(2\pi x_1) & 0 \\ 0 & 0 & 1 \end{pmatrix}.$$

Secondly, a way to rotate point z in some random direction is to project that point to random point p on the unit sphere. This projection is the same as a reflection through the plane, which is perpendicular to the line zp and contains the origin. This reflection is given by the Householder matrix

$$H = I - 2vv^T$$

where I is the unit matrix and v (v^T) is the (transposed) unit vector of the line zp . A projection has determinant -1 , but a rotation matrix should have a determinant of 1. A factor -1 can account for this and so the result becomes a valid random rotation matrix

$$M = -HR.$$

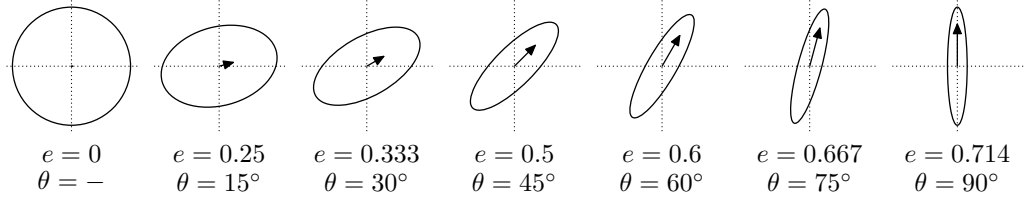


Figure A.1: Ellipses with different values for the ellipticity e and the direction ϕ .

The vector v is only defined as the unit vector of line zp . It can be given using the condition that matrix H should send point z to all other points on the unit sphere with equal probability. This is true when v takes the form

$$v = \begin{pmatrix} \cos(2\pi x_2) \sqrt{x_3} \\ \sin(2\pi x_2) \sqrt{x_3} \\ \sqrt{1 - x_3} \end{pmatrix}.$$

A.2 Ellipticity

In this section an algorithm is explained, which calculates the ellipticity of a certain distribution. This method is described in [17] and used in many articles, like [13]. For a distribution described by a $N \times N$ matrix M , the following moments can be calculated

$$\begin{aligned} \text{first moments} \quad \bar{x} &= \frac{1}{s} \sum_{i,j} x M_{ij} \\ &\bar{y} = \frac{1}{s} \sum_{i,j} y M_{ij} \\ \text{second moments} \quad Q_{xx} &= \frac{1}{s} \sum_{i,j} (x - \bar{x})^2 M_{ij} \\ Q_{xy} &= \frac{1}{s} \sum_{i,j} (x - \bar{x})(y - \bar{y}) M_{ij} \\ Q_{yy} &= \frac{1}{s} \sum_{i,j} (y - \bar{y})^2 M_{ij}, \end{aligned}$$

where $i, j = 1, 2, \dots, N$ and $s = \sum_{i,j} M_{ij}$.

The first moments correspond to the coordinates of the centre of mass of the distribution. The second moments contain information about the shape of the distribution. Note that all the moments are real valued. The ellipticity can be extracted from the second moments using the formula

$$e = \frac{Q_{xx} - Q_{yy} + 2iQ_{xy}}{Q_{xx} + Q_{yy} + 2\sqrt{Q_{xx}Q_{yy} - Q_{xy}^2}} = e_x + ie_y.$$

So the ellipticity can be represented as a vector in the complex plane. Its length $|e| = \sqrt{e_x^2 + e_y^2}$ is the magnitude of the ellipticity, where $e = 0$ is a circle and $e = 1$ is a line.

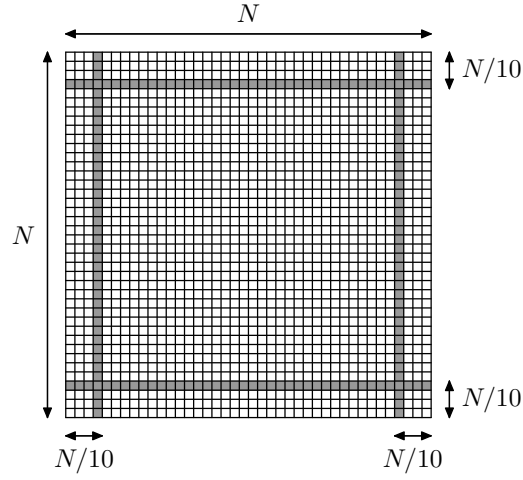


Figure A.2: Part of the distribution (grey) used to determine the threshold. The threshold is the maximum value of the four rows/columns which are $\frac{N}{10}$ pixels from the edge of a $N \times N$ distribution matrix.

In this report the term ellipticity will refer to this quantity, the absolute ellipticity. The direction of the ellipticity vector (given by $\arctan \frac{e_y}{e_x}$) is also the direction of the major axis of the ellipse. In figure A.1 some ellipses are shown for a range of values for the ellipticity.

With the use of the previous formulas, the ellipticity is related to the semimajor (a) and semiminor (b) axis and vice versa by

$$\begin{array}{ll}
 \text{ellipticity} & e = \frac{a-b}{a+b} \\
 \text{semimajor axis} & a = \frac{1+e}{1-e} b \\
 \text{semiminor axis} & b = \frac{1-e}{1+e} a .
 \end{array}$$

In general the edge of the convergence map only consists of a noisy background. In order to minimize the influence of this background, a selection of the total distribution is considered in the calculation. A certain threshold is subtracted from the distribution, after which only the positive values are selected to calculate the ellipticity. This threshold is the maximum value of the distribution at the four rows/columns which are $\frac{N}{10}$ pixels from the edges of the matrix. In figure A.2 is shown which values are taken into account in determining the threshold. Using this method, the background is omitted and so only the interesting part of the distribution is used in the calculation of the ellipticity.

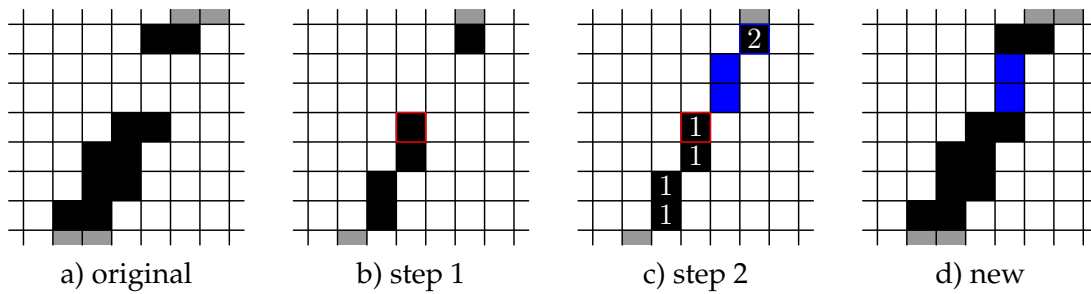


Figure A.3: The steps of the algorithm `FillGaps` which closes gaps in a curve contained in a binary matrix.

A.3 Algorithm `FillGaps`

The algorithm described in this section can be used when a binary (only values are zero and one) matrix M of size $N \times N$ contains a curve with gaps. An example is sketched in the leftmost image of figure A.3. In this case there is a gap of two pixels. There are a few steps to be taken to fill this gap and close the contour.

To begin with, the curve will be reduced to a line with a width of one pixel. To do so the MATLAB function `bwmorph` is used with the arguments `'skel'` and `1`. The MATLAB function is able to do morphological operations on binary images, or matrices in our case. The option `'skel'` stands for skeletonization and it removes pixels from the boundary until there is a line of one pixel left over. (The option `1` means that only one step is done.) After this, all the endpoints of the curve can be identified with the use of their property of having only one neighbour (out of eight). The skeletonization of M and finding the endpoints (in red) is depicted in figure A.3b).

For each endpoint, a 7×7 matrix m is extracted from the matrix M , with the endpoint at its centre. In this matrix m , connected pixels are identified using the algorithm `FindBlobs` (see appendix A.4). If there are pixels in matrix m not connected to the endpoint of interest, then these pixels are selected. The closest pixel will be chosen and an interpolating line is drawn between the endpoint and this pixel. The labelling of the region and the interpolation is shown in figure A.3c). The final step of the algorithm is to add the interpolated line to the original matrix M which is depicted again in the final image of figure A.3d). If matrix m contains only connected pixels around an endpoint, then the algorithm `FillGaps` stops.

This method will only interpolate gaps with a length of one or two pixels. Of course this bridging can be extended to bigger gaps by increasing the size of matrix m . But this can have the obvious drawback that the algorithm will connect line segments that should not be connected at all.

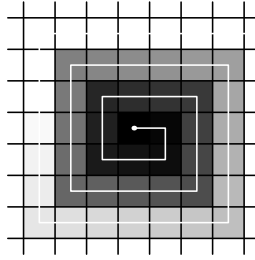


Figure A.4: The way of iterating through the matrix by algorithm `FindBlobs`.

A.4 Algorithm `FindBlobs`

This method is used to find all regions in a binary (only values are zero and one) matrix M . It is also called connected-component labelling. The result will be a matrix D (same size as M) in which each pixel contains the ID corresponding to the ID of the region, which it is part of. The algorithm will need one pixel to start with. From there it will find and define the regions.

The algorithm `FindBlobs` defines a vector called V , which plays a crucial role. In finding all the regions, pixels are investigated individually and given an ID using the sub-algorithm `FindID`. This sub-algorithm looks at the neighbours and subsequently assigns an existing ID or a new one. This will be explained at the end of this section. The permutation vector V keeps track of pairs of ID's that are connected and so should be the same. So if at some point it turns out that ID's d_i and d_j are connected, then the value $\min(d_i, d_j)$ is put at positions d_i and d_j of vector V . Vector V can be seen as a catalogue in which each pixel ID (each position in vector) is related to the lowest pixel ID in the same region (element of vector). In the end all old ID's d in matrix D are replaced by the new ID's d' by doing $d' = V(d)$. So then all regions have one ID and eventually the region can be renumbered as a consecutive sequence.

Many algorithms for finding connected components have to iterate over the whole matrix. But the algorithm `FindBlobs` starts at some given pixel and then spirals out, while investigating each pixel as shown in figure A.4. The reason for this is that the regions are often not spread around the matrix, but more likely to be in a cloud. When starting in the centre of this cloud, the algorithm can be stopped if all pixels in the cloud (all ones in M) have been labelled with an ID.

Now a bit more detailed description will be given of the main and essential steps of the algorithm `FindBlobs`, followed by the sub-algorithm `FindID`

- The algorithm starts at the given starting point with assigning an ID, using the sub-algorithm `FindID`.

- After that, all pixels are investigated until all ones have been found. For each pixel in a region, the sub-algorithm `FindID` is ran to define all ID's.
- When all necessary pixels in M have an ID then the permutation vector V is finalized by doing $V = V(V)$ until it does not change any more.
- Then all ID's in matrix D are put into V to get the final ID's, which are stored back in D again.
- Finally all regions contain only one ID and subsequently they can be renumbered to get a serie of consecutive ID's.

Sub-algorithm FindID — This algorithm is executed for all pixels for which $M = 1$ and so they need an ID d' . To find this value, the following steps have to be taken.

- Collect all ID's d_i that are already assigned to the eight neighbouring pixels.
 - If there are ID's d_i from the surrounding pixels, then the final ID of the pixel of interest is $d' = \min(d_i, V(d_i))$. Also the vector V should be updated by evaluating $V(d_i, V(d_i)) = d'$.
 - If there are no d_i , then a new ID is assigned to d' , which will also be added to the vector V by $V(d') = d'$.

A little note on the efficiency of this algorithm is in place. `FindBlobs` is not the quickest algorithm for finding connected regions in all situations and programming languages. But MATLAB (version 2012a) could accelerate `FindBlobs` (with the use of the JIT-accelerator) which made it quicker than the method given in [18], for example (which was not accelerated in MATLAB). The method in the article was used to check the algorithm `FindBlobs`.

B

Supplementary tables and figures

In this chapter some supplementary tables and figures will be presented. What is exactly shown will be explained in the following lists, one for each section in this appendix.

B.1	Rotations
Figure B.1	The distributions and correlation plots of the total, tangential and radial caustic area with the ellipticity for the CDM cluster.
Figure B.2	The distributions of the shear parameters and the correlations of these parameters with the ellipticity, where the shear of the outer region of both the CDM and WDM cluster is used.
B.2	Magnification probability distribution
Figure B.3	The convergence, caustics and critical lines of the CDM cluster orientation for which the maximum convergence is maximal.
Figure B.4	The convergence, caustics and critical lines of the CDM cluster orientation for which the caustic area of more than 5 images is maximal.
Figure B.5	Probability distributions for a very small source.
Figure B.6	Probability distributions for a very big source.

B.1 Rotations

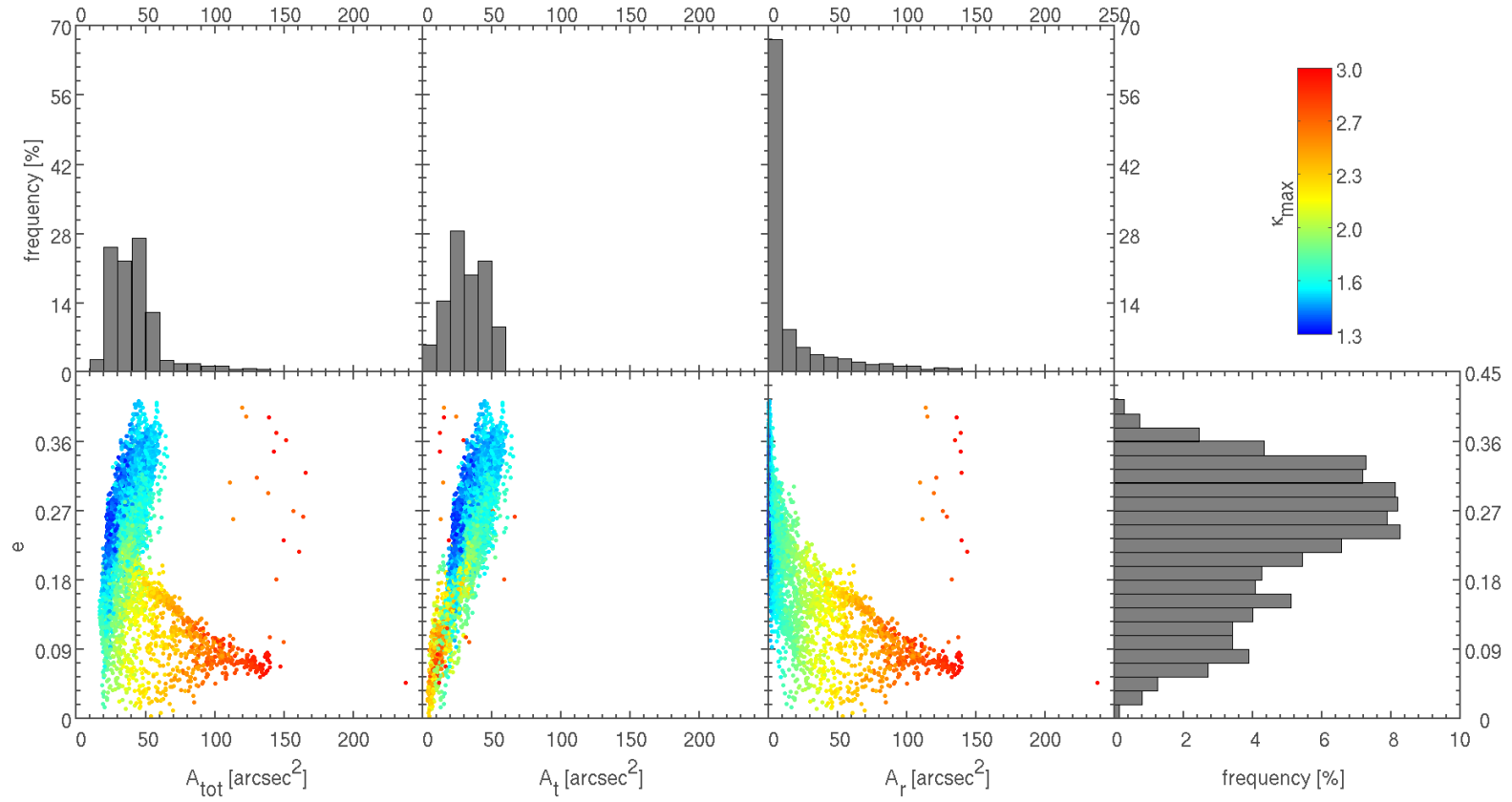


Figure B.1: The distributions (top row) and correlation plots (bottom) of the total (first column), tangential (second column) and radial caustic area (third column) with the ellipticity for the CDM cluster. The bottom most right plot shows the distribution of the ellipticity. The colour coding of the points represents the maximum convergence.

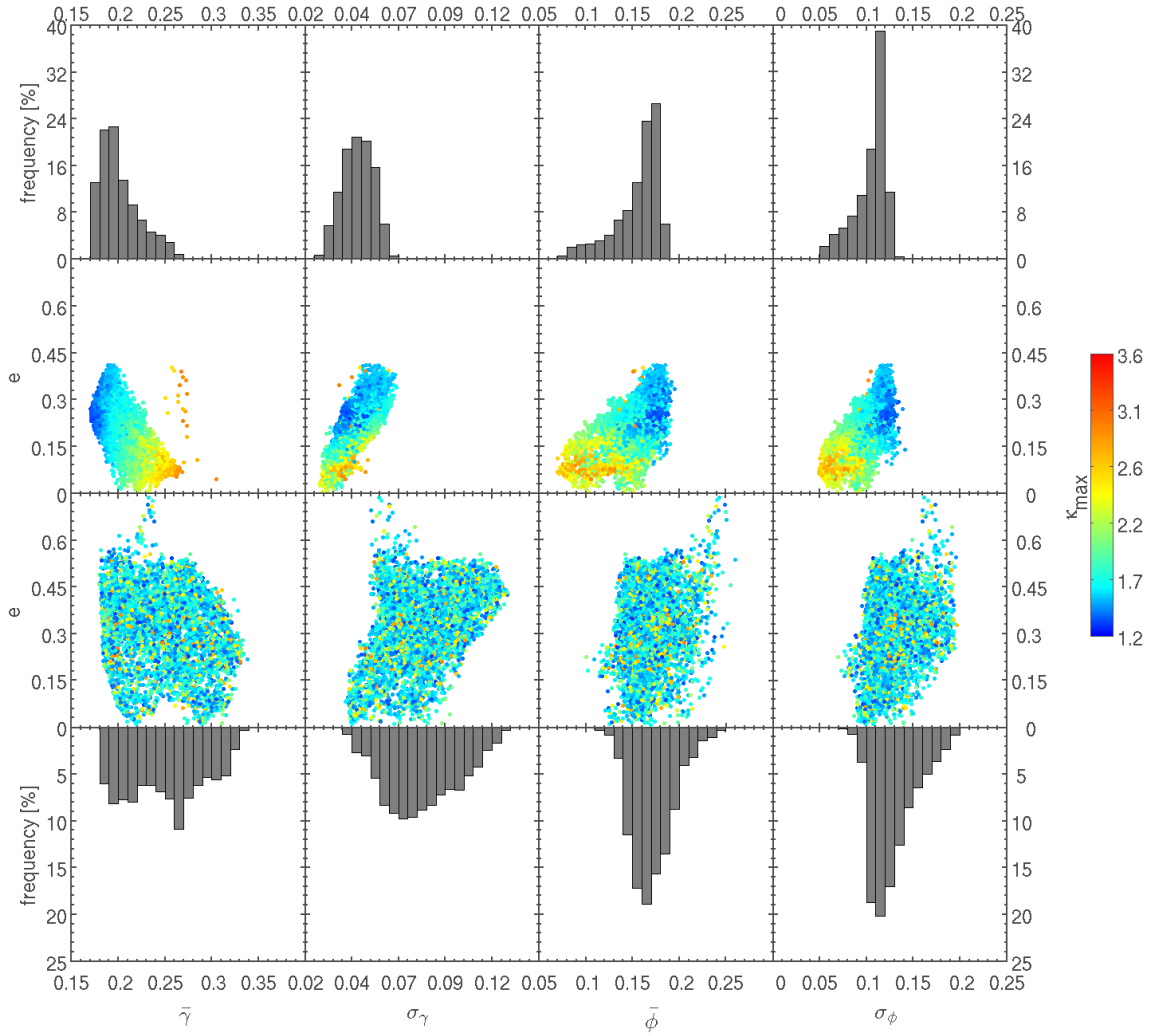


Figure B.2: The distributions of the shear parameters (top row) and the correlations of these parameters with the ellipticity (second row), where the shear of the outer region of the CDM cluster is used. Analogously the WDM cluster results are presented in the two bottom rows. The colour coding of the points represents the maximum convergence.

B.2 Magnification probability distribution

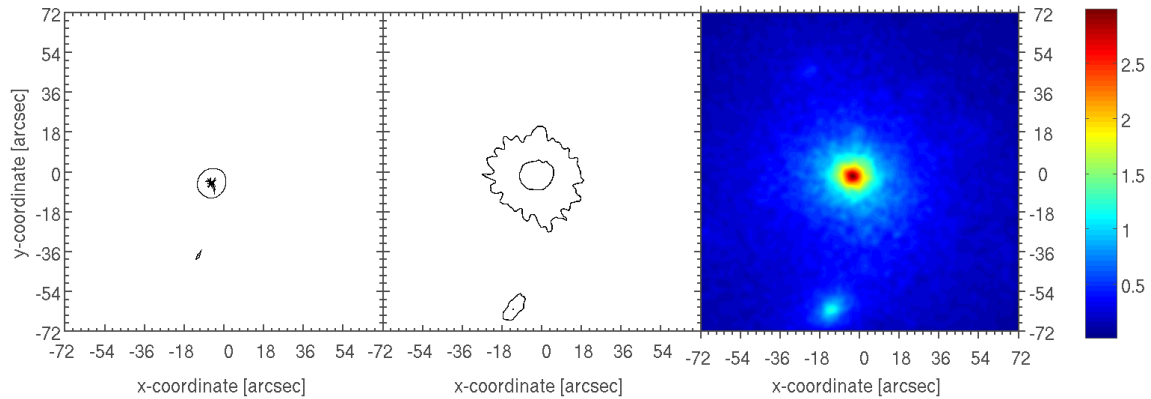


Figure B.3: The convergence of the inner region (right), the caustics (left) and the critical lines (middle) for the orientation of the CDM cluster for which the maximum convergence is maximal.

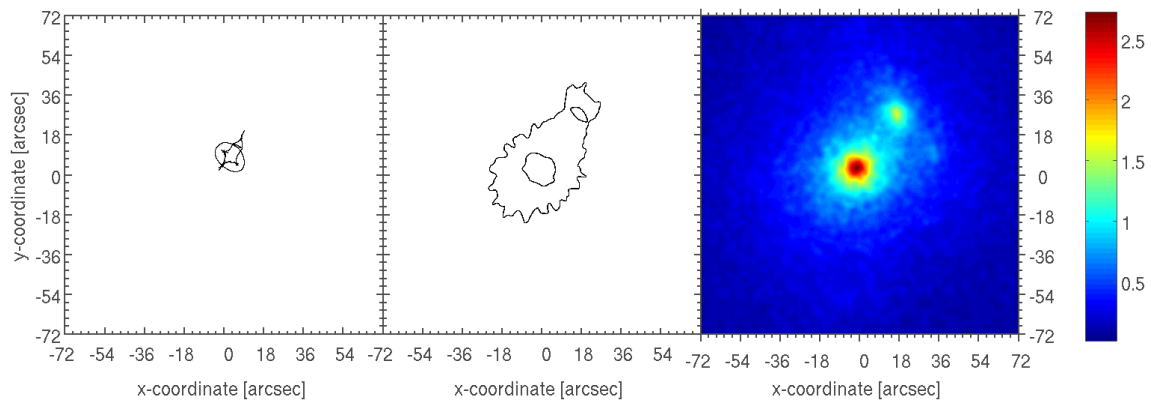


Figure B.4: The convergence of the inner region (right), the caustics (left) and the critical lines (middle) for the orientation of the CDM cluster for which the caustic area of more than 5 images is maximal.

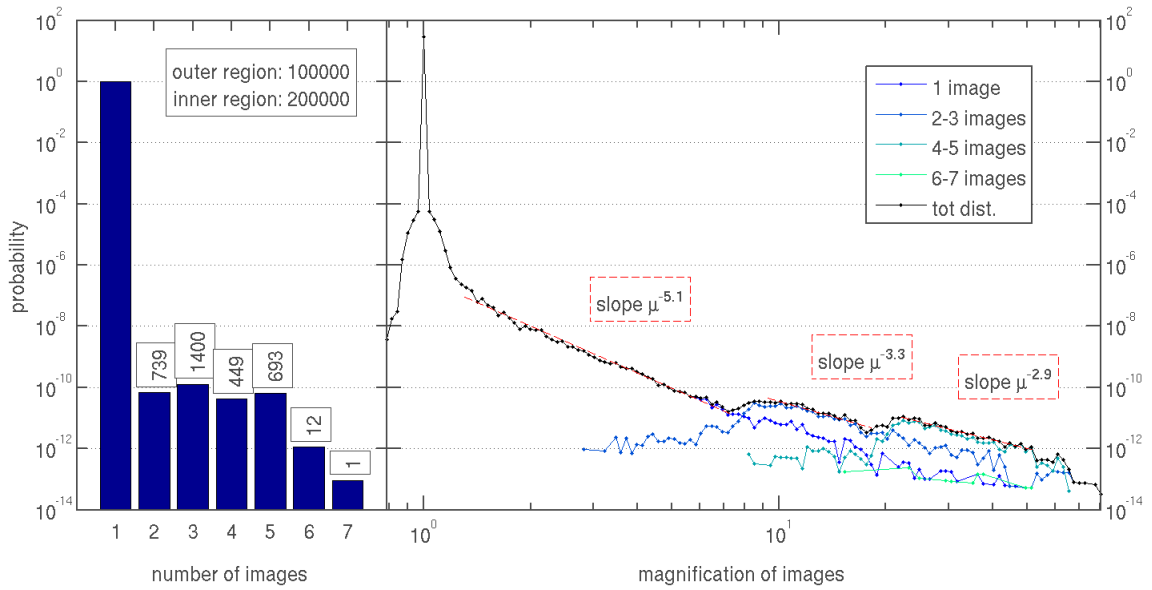


Figure B.5: Probability of a very small source ($A_s = 30$ pix) producing some number of images (left) and the source magnification probability distribution (right) for the rotation of the CDM cluster for which the caustic area of more than 5 images, A_5 , is maximal.

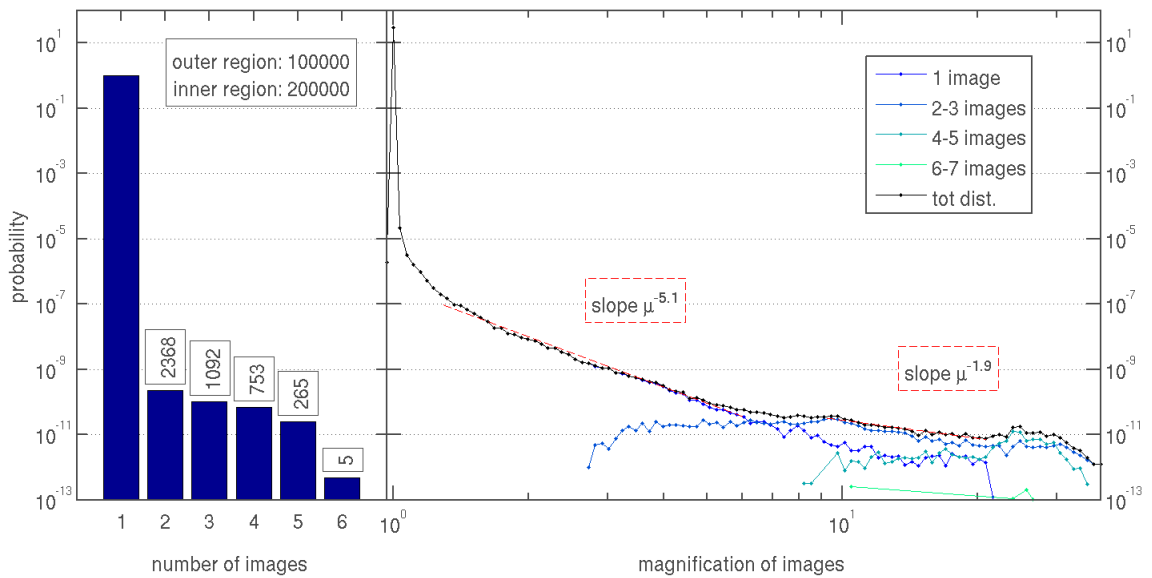


Figure B.6: Probability of a very big source ($A_s = 360$ pix) producing some number of images (left) and the source magnification probability distribution (right) for the rotation of the CDM cluster for which the caustic area of more than 5 images, A_5 , is maximal.